



1 **A fully autonomous ozone, aerosol and night time water**
2 **vapor LIDAR: a synergistic approach to profiling the**
3 **atmosphere in the Canadian oil sands region**

4

5 **Kevin B. Strawbridge¹, Michael S. Travis¹, Bernard J. Firanski¹, Jeffrey R.**
6 **Brook¹, Ralf Staebler¹ and Thierry Leblanc²**

7 [1]{Air Quality Processes Research Section, Environment and Climate Change Canada,
8 Toronto, ON, Canada}

9 [2]{ California Institute of Technology, Jet Propulsion Laboratory, Wrightwood, CA 92397,
10 USA.}

11 Correspondence to: Kevin B. Strawbridge (Kevin.Strawbridge@canada.ca)

12 **Abstract**

13 LIDAR technology has been rapidly advancing over the past several decades. It can be used
14 to measure a variety of atmospheric constituents at very high temporal and spatial resolutions.
15 While the number of LIDARs continues to increase worldwide, there is generally a
16 dependency on an operator, particularly for high-powered LIDAR systems. Environment and
17 Climate Change Canada (ECCC) has recently developed a fully autonomous, mobile LIDAR
18 system called AMOLITE (Autonomous Mobile Ozone LIDAR Instrument for Tropospheric
19 Experiments) to simultaneously measure the vertical profile of tropospheric ozone, aerosol
20 and water vapor (night time only) from near ground to altitudes reaching ten to fifteen
21 kilometers. This current system uses a dual laser, dual LIDAR design housed in a single
22 climate-controlled trailer. Ozone profiles are measured by the Differential Absorption
23 LIDAR (DIAL) technique using a single 1 m Raman cell filled with CO₂. The DIAL
24 wavelengths of 287 nm and 299 nm are generated as the second and third Stokes lines
25 resulting from stimulated Raman scattering of the cell pumped using the fourth harmonic of a
26 Nd:YAG laser (266nm). The aerosol LIDAR transmits three wavelengths simultaneously
27 (355 nm, 532 nm and 1064 nm) employing a detector designed to measure the three
28 backscatter channels, two nitrogen Raman channels (387 nm and 607 nm), and one cross-
29 polarization channel at 355 nm. In addition, we have added a water vapor channel arising
30 from the Raman-shifted 355nm output (407nm) to provide nighttime water vapor profiles.



1 AMOLITE participated in a validation experiment alongside four other ozone DIAL systems
2 before being deployed to the ECCO Oski-ôtin ground site in the Alberta Oil Sands region in
3 November 2016. Ozone was found to increase throughout the troposphere by as much as a
4 factor of 2 from stratospheric intrusions. A biomass burning event that impacted the region
5 over an eight-day period produced LIDAR ratios of 35 to 65 sr at 355 nm and 40 to 100 sr at
6 532. Over the same period the Angstrom exponent decreased from 1.56 ± 0.2 to 1.35 ± 0.2
7 between the 2 to 4 km smoke region. The advantage of nearly continuous measurements
8 obtained over a 12-month period will be presented, highlighting the synergistic advantage of
9 AMOLITE's tri-LIDAR design.

10



1 **1 Introduction**

2 Tropospheric ozone, aerosols and water vapor are important atmospheric constituents
3 affecting air quality and climate. Ozone is a short-lived climate pollutant (SLCP) and air
4 pollutant that can have detrimental impacts on human health (Malley et al., 2015, Lippmann,
5 1991), agriculture (McKee, 1994) and ecosystems (Ashmore, 2005) when present at high
6 enough concentrations. Tropospheric ozone is photo-chemically produced primarily from
7 nitrogen oxides and volatile organic compounds (VOCs) from anthropogenic sources,
8 biogenically produced from forest fires (Aggarwal et al., 2017 and Trickl et al., 2015) and can
9 be enhanced through stratospheric/tropospheric transport (STT) events (Ancellet et al., 1991,
10 Langford et al., 1996, Leblanc et al., 2011 and Trickl et al., 2014). Both of these latter
11 sources can have significant impacts on ozone concentration although typically their impacts
12 vary within the vertical distribution of the troposphere. The advantage of ozone DIAL is the
13 ability to measure this vertical column with high enough temporal resolution to understand
14 atmospheric mixing and processes. Along with ozone, the vertical distribution of aerosols can
15 also vary considerably throughout the troposphere.

16 Aerosols or particulate matter are tiny particles suspended in the air which contribute to the
17 radiative budget, are a tracer for pollution transport and impact visibility, cloud formation and
18 air quality. They affect the earth's climate by interacting with the sun and earth's radiation
19 (Ramanathan, 2001) and by modifying clouds (Feingold et al., 2003 and Twomey, 1977) and
20 depending on their size and the meteorological conditions can travel great distances around
21 the globe (Uno et al., 2009). In high enough concentrations these particles can have dramatic
22 effects on visibility (Li et al., 2016 and Singh, 2017) and cause respiratory problems,
23 particularly in those suffering from lung conditions such as asthma. This has been the
24 motivation for several countries to adopt an air quality index (Kousha et al., 2015) to alert the
25 public to respiratory dangers during pollution events. Aerosol backscatter LIDAR systems
26 are uniquely capable of providing the vertical profile of tropospheric aerosols at very high
27 temporal and spatial resolutions and are therefore ideal instruments to study the aerosol
28 processes outlined above. While the vertical distribution of ozone and aerosols can be highly
29 variable throughout the troposphere, water vapor tends to have the highest concentration
30 closest to the surface and throughout the mixed layer.

31 Water vapor plays a pivotal role in climate change and atmospheric stability by directly
32 influencing many atmospheric processes such as cloud formation (Pruppacher and Klett,



1 1997) and photochemical atmospheric reactions (Yamamoto et al., 1966 and Grant, 1991).
2 Furthermore, tropospheric water vapor is a catalyst to many atmospheric chemical reactions
3 by functioning as a solvent for chemical products of natural and anthropogenic activities
4 (Grant, 1991). Also, as one of the primary greenhouse gases, with strong infrared absorption
5 in the 100-600 cm^{-1} spectral region, water vapor helps to maintain the earth's radiation
6 balance by absorbing and emitting infrared radiation (Twomey, 1991, Clough et al., 1992 and
7 Sinha and Harries, 1995).

8 The purpose of this paper is to describe a vertical profile measurement system that measures
9 ozone, aerosols and water vapor simultaneously. By employing three different LIDAR
10 techniques - Mie backscatter LIDAR, water vapor Raman LIDAR and ozone DIAL - in one
11 observation platform we are able to explore a synergistic approach to advance our
12 understanding of lower atmospheric dynamics with the eventual goal of supporting
13 development to improve air quality forecasts, diagnostic models and satellite measurements.
14 There are only a few sites that currently exist where all three LIDAR techniques are operated:
15 Garmisch-Partenkirchen Zugspitze (Trickl et al., 2015), Maïdo observatory Reunion Island
16 (Baray et al., 2013) and Observatoire de Haute-Provence (OHP) (Bock et al., 2013, Khaykin
17 et al., 2017 and Gaudel et al., 2015). However, all of these sites are high altitude sites that
18 began as stratospheric observatories.

19 The accomplishment here was to develop such a platform to be mobile and to run
20 autonomously providing near continuous observations (except during precipitation events),
21 even in remote areas. Environment and Climate Change Canada (ECCC) has designed and
22 built a fully autonomous, mobile LIDAR system, based on the backbone of an earlier system
23 design (Strawbridge, 2013), named AMOLITE (Autonomous Mobile Ozone LIDAR
24 Instrument for Tropospheric Experiments) to simultaneously measure the vertical profile of
25 tropospheric ozone, aerosol and water vapor. To verify the system's performance AMOLITE
26 participated in a validation campaign known as the Southern California Ozone Observation
27 Project (SCOOP) at the Jet Propulsion Laboratory's Table Mountain Facility in Wrightwood,
28 CA during August, 2016. This study brought together five of the six tropospheric ozone
29 LIDARs that form the Tropospheric Ozone LIDAR Network – TOLNet (- [http://www-
30 air.larc.nasa.gov/missions/TOLNet/](http://www-air.larc.nasa.gov/missions/TOLNet/)). In addition to the five LIDARs, ozone sonde balloons
31 were launched throughout the study period. This campaign provided an excellent opportunity
32 to evaluate the ozone profiles produced by AMOLITE. For details of the inter-comparison



1 refer to a separate publication (manuscript in preparation). LIDAR networks are very
2 important scientific tools that allow the collective benefit of increased geographical coverage
3 (Langford et al., 2018 and Trickl et al., 2016) and can often provide valuable climatological
4 data (Granados-Munoz et al., 2016, Khaykin et al., 2017 and Gaudel et al., 2015). It has also
5 been shown in the recent Tropospheric Ozone Assessment Report (TOAR) by Gaudel et al.,
6 (2018) the lack of ozone profilers in the troposphere to further support the existence of
7 networks like TOLNet.

8 After the validation campaign, AMOLITE was shipped back to Canada where it was made
9 ready for deployment to the oil sands region. AMOLITE first light ozone and water vapor
10 profiles were acquired on 3 November 2016 at the Oski-ôtin ground site in Fort McKay, AB.
11 In addition to the LIDAR measurements, operation of a windRASS (wind radio-acoustic
12 sounding system – model MFAS, Scintec, Rottenburg, Germany) provides the local
13 meteorological wind fields at 10m vertical resolution from 40 m to typically 500m above
14 ground, directly determining the upwind sources near ground level and aloft over the site.
15 These remote sensors provide a coherent 3D picture of the transport processes impacting the
16 ground site and the region nearby. Also housed in a trailer on site is a facility called CAM1
17 (good reference here for CAM1) that has an extensive suite of ground-based instrumentation
18 that continuously measures a variety of gaseous and particulate pollutants. The purpose of
19 this site is to identify the predominant sources impacting the region and the main local-scale
20 atmospheric processes influencing pollutant transport, transformation and deposition. This
21 information will be used to improve our knowledge of what is being emitted and the
22 processes in the atmosphere that affect where the pollutants move and deposit.

23 The focus of this paper will be on the additional development required to add the ozone and
24 water vapor capability to the previous autonomous aerosol LIDAR design developed by
25 ECCCC, followed by a brief section on the validation and verification of the instrument and
26 processing algorithms. The fourth section will describe a few case studies acquired
27 throughout the first year of operation at the Oski-ôtin ground site in Fort McKay. The final
28 section will draw conclusions and discuss some future improvements that are currently
29 underway for AMOLITE.

30



1 2 LIDAR technique

2 In this paper we are using three different LIDAR techniques to measure different atmospheric
3 constituents: a Mie backscatter LIDAR to measure the vertical profile of aerosol at three
4 different wavelengths, a Differential Absorption LIDAR (DIAL) to measure the vertical
5 ozone profile and a Raman LIDAR to measure water vapor profile. The Mie backscatter
6 aerosol lidar technique employed in AMOLITE, has already been described in detail by
7 Strawbridge, 2013. Here we briefly describe the DIAL and Raman LIDAR techniques used
8 for the systems in AMOLITE.

9 2.1 Ozone DIAL Technique

10 Using the DIAL technique, it is possible to retrieve ozone mixing ratios from the backscatter
11 profiles. The technique essentially uses the differential absorption of ozone at two different
12 wavelengths that are relatively close together to minimize aerosol effects, but far enough apart
13 to have a large difference in their ozone absorption cross sections. Consequently, the ozone
14 calculation uses the two-wavelength solution of the lidar equation given below (Kovalev et
15 al., 1994):

$$16 \quad N(z) = \frac{-1}{2(\alpha_{on} - \alpha_{off})} \left[\frac{d}{dz} \left[\ln \frac{P_{on}(z)}{P_{off}(z)} - \ln \frac{B_{on}(z)}{B_{off}(z)} \right] + 2\Delta\sigma(z) \right] \quad (1)$$

17

18 where

19 $\alpha_{on} - \alpha_{off}$ is the differential ozone absorption, $\frac{P_{on}(z)}{P_{off}(z)}$ is the signal ratio, $\frac{B_{on}(z)}{B_{off}(z)}$ is the backscatter
20 ratio and $2\Delta\sigma(z)$ is the total two-way scatter or extinction differential. In our system the signal
21 at 287 nm representing the “on” signal and 299 nm representing the “off” signal. Solving for
22 the component of the backscatter due to the molecular contribution and the aerosol
23 contribution, it is possible to express the backscatter contribution overall to the ozone
24 calculation at the on and off wavelengths based solely on the ratio between the aerosol and
25 molecular backscatter at some reference wavelength, referred to by Kovalev as the backscatter
26 ratio $S(z)$. This is represented by



$$\frac{B_{on}(z)}{B_{off}(z)} = \frac{1 + S(z, \lambda_{rsf}) \left(\frac{\lambda_{on}}{\lambda_{rsf}} \right)^{4-\nu}}{1 + S(z, \lambda_{rsf}) \left(\frac{\lambda_{off}}{\lambda_{rsf}} \right)^{4-\nu}} \quad (2)$$

1
2 Where ν is the Angstrom exponent representing the wavelength dependence of aerosol Mie
3 backscatter and in our case the reference wavelength is 355 nm. In the case of AMOLITE a
4 boxcar filter is used to produce a simple smoothing of the raw data followed by a second-
5 order Savitzky-Golay convolution. Although the Savitsky-Golay approach may cause issues
6 at the top of the stratospheric ozone profiles (Godin et al., 1999) it does not have as much of a
7 negative impact for tropospheric ozone due to the vertical structure of ozone typically
8 increasing at the top of the profile. This is primarily due to the signal-to-noise ratio being
9 large enough at most altitudes. Alternate, more sophisticated filters are being considered and
10 may be implemented in future data versions, but for now all TOLNet LIDARs are using the
11 same approach. Tropospheric ozone DIAL along with water vapour LIDAR can provide
12 complimentary datasets when investigating transport or process studies.

13 2.2 Water Vapor Raman Technique

14 During the early stages of the optical detector design for the aerosol LIDAR, it was
15 determined that with the addition of a few optics it would be possible to measure nighttime
16 water vapor using the Raman technique on the 355 nm laser wavelength. This would be
17 particularly valuable when identifying STT events where the dry stratospheric air can be
18 easily identified by the water vapor LIDAR measurements (Trickl et al., 2014). Raman
19 scattering is an inelastic quantum-mechanical scattering process, in which the wavelength of
20 the incident radiation is shifted as a result of the interaction of the photons with target
21 molecules. The Raman wavelength shift, related to the exciting laser wavelength (λ_L), is
22 proportional to the distinct ro-vibrational energy levels and provides a unique fingerprint for
23 each molecule. In the framework of perturbation theory, Raman scattering corresponds to the
24 absorption and subsequent emission of a photon via an intermediate electronic state, which is
25 based on the target molecule ro-vibrational states, producing either a longer (Stokes) or
26 shorter (anti-Stokes) wavelength shift. Most atmospheric species are vibrationally active;
27 resulting in a net Raman shift to longer wavelengths ($\lambda_r > \lambda_L$), which indicates that atmospheric
28 target molecules gain energy from the radiation field. The most probable Raman shifts for N_2



1 and H_2O are at 2330.7 cm^{-1} and 3652.0 cm^{-1} , respectively (Whiteman et al., 1992).
 2 Theoretically, Raman wavelength (λ_r) is related to the Raman shift (κ in cm^{-1}) by

$$3 \quad \frac{1}{\lambda_r} = \frac{1}{\lambda_L} - \kappa \quad (3)$$

4 The general lidar equation for Mie-Rayleigh elastic backscattering for a given incident laser
 5 wavelength (λ) is given by (Whiteman, 2003)

$$6 \quad P(z, \lambda) = P_o \frac{c\tau}{2} \frac{A}{z^2} \eta^* O(z) \beta(z, \lambda) \exp\{-2\int \alpha(z', \lambda) dz'\} \quad (4)$$

7 where P_o is the average power of a single laser pulse, τ is temporal pulse length of the laser, A
 8 is the detector area, η is the overall system efficiency (optical transmission from emitter to
 9 receiver and detection efficiency). $O(z)$ is the geometry factor containing the overlap function
 10 of the laser beam with the receiver field-of-view, β is the backscatter coefficient, which is the
 11 parameter that determines the strength of the signal being received by the telescope and the
 12 exponential term represents the two-way transmission loss as the laser propagates through the
 13 atmosphere where $\alpha(z)$ is the volume extinction coefficient due to molecular and aerosol
 14 contributions (Wandinger, 2005). For inelastic scattering process, Equation (4) above can be
 15 modified into

$$16 \quad P(z, \lambda_l, \lambda_r) = P_o(\lambda_l) \frac{k^*}{z^2} O(Z) \beta(Z, \lambda_l, \lambda_r) \exp\left\{-\int_0^z [\alpha_l(\lambda_l, z') + \alpha_r(\lambda_r, z')] dz'\right\} \quad (5)$$

17 where k^* is the lidar calibration constant, and α_l and α_r refer to the extinction coefficients (m^{-1})
 18 resulting from the incident and Raman wavelengths, respectively (Aspey, et al., 2006). When
 19 the Raman backscatter coefficient is expressed in terms of the scattering cross section ($d\sigma/d\omega$
 20 in $m^2 \cdot molecule^{-2} \cdot sr^{-1}$) of water vapor and nitrogen molecules and multiplied by the molecular
 21 number density $N(z)$ as (Aspey et al., 2006 and Ansmann, 1990) one gets

$$22 \quad \beta(z, \lambda_l, \lambda_r) = N_r(z) \frac{d\sigma(\lambda_l, \lambda_r)}{d\Omega} \quad (6)$$

23 Substituting Eq.(6) into Eq. (5), and taking the ratio between the water vapor and nitrogen
 24 Raman signals, yields a mathematical expression for the dependence of Raman signals ratio
 25 on water vapor and nitrogen molecular density (N_{H_2O} and N_{N_2}), namely

$$\frac{P(z, \lambda_l, \lambda_{H_2O})}{P(z, \lambda_l, \lambda_{N_2})} \propto R \frac{N_{H_2O}}{N_{N_2}} \frac{[d\sigma_{H_2O}/d\Omega]}{[d\sigma_{N_2}/d\Omega]} \exp\left\{-\int_0^z [\alpha(\lambda_{H_2O}, z') - \alpha(\lambda_{N_2}, z')] dz'\right\} \quad (7)$$



1

2 where R is the proportionality constant dependent on the instrument specifications. This
3 equation ignores the temperature-dependent functions required for very narrow bandwidth
4 filters, typically used for daytime operation (see Whiteman, 2003).

5 The water vapor mixing ratio (WVMR denoted as $w(z)$) in grams of water vapor per
6 kilogram of dry air) as a function of vertical altitude (z) is proportional to the ratio of the
7 number density of water vapor to nitrogen, and is given by (Goldsmith et al., 1998):

$$8 \quad w(z) = \frac{MW_{H_2O} N_{H_2O}(z)}{MW_{DryAir} N_{DryAir}(z)} \approx \frac{MW_{H_2O} N_{H_2O}(z)}{MW_{DryAir} N_{N_2}(z)/0.78} \approx 0.485 \frac{N_{H_2O}(z)}{N_{N_2}(z)} \quad (8)$$

9 The WVMR equation above can be related to experimentally recorded Raman lidar signals by
10 comparing Eqs. (7) and (8), leading to the following expression

$$11 \quad w(z) = D \frac{S_{H_2O}}{S_{N_2}}, \quad (9)$$

12 where D (in g/kg) is a constant depending on instrumental specifications, ratio between N_2
13 and H_2O backscattering cross sections, N_2 mixing ratio, and Raman lidar signals extinction
14 due to the aerosols and air molecules (Dionisi et al., 2009). The D constant is commonly
15 evaluated by comparison with independent measurement (radiosonde) of water vapor mixing
16 ratio ($w(z)$).

17

18 **3 AMOLITE system design**

19 **3.1 Trailer Design and Infrastructure**

20 The current system described here builds upon the successes of the autonomous aerosol
21 LIDARS built over the past decade by ECCC (Strawbridge, 2013). AMOLITE uses a
22 synergistic approach which combines a dual laser (for redundancy), dual LIDAR design
23 (tropospheric ozone DIAL (Differential Absorption LIDAR and aerosol LIDAR) housed in
24 the same trailer. In order to accommodate two LIDAR systems, the trailer needed to be
25 slightly larger interior footprint of 2.1 m by 4.3 m feet long. A picture of AMOLITE,
26 operating in full autonomous mode, deployed on a field experiment is shown in Figure 1a.
27 The external infrastructure of the trailer was very similar to previous designs utilizing a



1 meteorological tower, precipitation sensor enabled hatch cover, modified vertically-pointing
2 radar interlock system and the other safety equipment required for operation of a class IV
3 laser. The main differences in the design were the addition of a second radome to provide
4 safety radar redundancy, larger hatch opening to allow the operation of two LIDAR receivers
5 simultaneously and a greatly improved heating and cooling system. The second radar system
6 allows one to remotely change between radar sources in the event that a system failure occurs.
7 We found that these radomes would typically last between 2 and 4 years. However, when a
8 failure occurs the LIDAR system is shut down for safety reasons until a site visit can be
9 arranged and a new radar system installed. The addition of a second radar reduced system
10 downtime and operational costs. The larger hatch not only is necessary for dual-LIDAR
11 operation, but was also modified to allow the wiper system to operate while the hatch is either
12 open or closed. It was also designed to accommodate exterior blower fans to prevent the
13 accumulation of insects on the window attracted by the UV laser light. The most significant
14 upgrade was the addition of two Mitsubishi Mr. Slim ducted units capable of delivering
15 between 6000 and 24000 BTU of cooling with external temperatures as low as -40C as well
16 as heat units mounted in the duct. The ducting allows for better distribution of cool and warm
17 air, maintaining a much more thermally stable environment throughout all the seasons of
18 operation. The internal infrastructure of the trailer followed the early design of rack-mounted
19 components and a single optical bench. The optical bench layout (see Figure 1b) was large
20 enough to mount both LIDAR systems including the two laser sources per LIDAR. The main
21 improvements on the internal workings of the trailer infrastructure were the inclusion of a
22 battery-operated propane furnace and charger capable of maintaining trailer heat for at least
23 48 hours in the event of a power failure. This is particular important should there be a power
24 failure during the winter season, which can leave the trailer without heat for hours at a time
25 causing the laser coolant to freeze, resulting in severe damage to the lasers. The other major
26 change was the analog to digital computer card with a modular Advantech ADAM I/O system
27 with greater flexibility and robustness. These improvements to the trailer infrastructure
28 provided a more stable, reliable environment for improved data quality and uptime.

29 **3.2 Aerosol LIDAR design**

30 Since the aerosol LIDAR design described in Strawbridge, 2013 was the backbone of this
31 new system only the changes will be discussed. The main differences are adding a laser for
32 redundancy and adding an additional transmitted wavelength (355 nm) which in turn added



1 the ability to acquire more particle information and a water vapor channel arising from the
2 Raman shifted 355 nm output (407 nm) to provide night time water vapor profiles. The
3 second identical laser, a Continuum Inlite III Nd:YAG operating at 20 Hz (see Figure 1b),
4 shares the same steering mirror (see Figure 2) as the primary laser and can therefore be
5 engaged remotely by a computer-controlled interface. The folding mirrors and steering mirror
6 are a triple-coated (anti-reflection coating at 355 nm, 532 nm and 1064 nm) 50 mm optic
7 mounted in a Thorlabs mount with encoded Thorlab actuators to permit remote alignment if
8 necessary. A schematic of the aerosol LIDAR in Figure 2 shows the transmitter beam path
9 and receiver design. The receiver was designed to image the aperture on the photomultiplier
10 tube rather than the field stop. This is necessary to avoid signal modulations due to the
11 inhomogeneous sensitivity of the cathode. The Continuum laser has an output energy of at
12 least 65 mJ at 355 nm, 65 mJ at 532 nm and 100 mJ at 1064 nm. The seven-channel receiver
13 (see Figure 2) measures the backscatter at each of the emitted wavelengths as well as the
14 depolarization at 355 nm, the nitrogen Raman channels at 387 nm and 607 nm and the water
15 vapor Raman channel at 407 nm. All of the channels, except the 1064 nm channel, use
16 LICEL photomultiplier tubes coupled into a LICEL analog/photon counting transient recorder
17 to increase the dynamic range. The 1064 nm channel is focused onto a Perkin Elmer
18 C30956E avalanche photodiode (APD). The APD incorporates a logarithmic amplifier
19 (25mV rms noise), made by Optech Inc., to increase dynamic range. The amplifier was
20 calibrated prior to the experiment via a transfer function, to convert the signal to a linear
21 scale, in addition to second-order corrections provided by Optech Inc. The signal is directed
22 into a 14-bit, Gage Compuscope computer card. Both the LICEL transient recorder and Gage
23 computer card were externally triggered by the same Stanford Research delay generator. The
24 collected data is averaged to produce aerosol profiles from 100 m to 15 km agl every minute
25 and water vapor profiles from 100 m to 10 km agl every 5 minutes.

26 **3.3 Ozone DIAL design**

27 The ozone DIAL system optical bench layout and detector design is shown in Figure 3. A
28 dual laser design is also used for redundancy and can be engaged remotely by a user
29 controlled translation stage that moves the folding mirror in and out of the optical axis of the
30 transmitter. The folding mirrors have an anti-reflection coating at 266 nm. The lasers are
31 Continuum Inlite III Nd:YAG operating at 20 Hz with an output energy specification of 45
32 mJ. The laser pumps a 1 m long CO₂-filled Raman cell (Nakazato et al., 2007) manufactured



1 by Light Age. The multi-wavelength output from the Raman cell is directed zenith by a
2 steering mirror that is broadband coated from 266 nm to 320 nm. This 50 mm optic mounted
3 in a Thorlabs mount with encoded Thorlab actuators has a user-controlled interface to permit
4 remote alignment if necessary. The differential pair chosen for the DIAL is the second and
5 third Stokes lines from the Raman conversion, namely 287 nm and 299 nm. The two
6 wavelengths are separated out via the detector block where the signals from the LICEL
7 photomultiplier tubes are directed into a LICEL analog/photon counting transient recorder.
8 Again the optical design imaged the aperture onto the photomultiplier tube for the same
9 reason discussed in section 3.2. A slight delay is imposed on the DIAL Stanford Research
10 delay generator to minimize cross-talk between the two LIDAR systems. The single
11 telescope design is capable of measuring ozone as low as 400 m above ground level (agl) to
12 altitudes reaching 15 km during the night every 5 minutes. It operates 24 hours a day, seven
13 days a week except during precipitation events. The system is operated remotely and the data
14 are updated hourly to a website providing near real-time capability.

15 **3.4 AMOLITE Instrument Validation and Calibration**

16 The performance of the ozone LIDAR was evaluated through an inter-comparison study with
17 four other tropospheric ozone LIDARs, all of which are part of TOLNet (Tropospheric Ozone
18 LIDAR Network). The campaign named SCOOP (Southern California Ozone Observation
19 Project) took place at the JPL Table Mountain Facility in Wrightwood, California. This
20 provided an opportunity to compare LIDAR ozone profiles between other LIDAR instruments
21 and 14 ozone sondes launched during the study. The vertical resolution of the ozone LIDAR
22 was chosen to be range dependent to provide sufficient detail in the lower troposphere as well
23 as providing ozone profile information to altitudes reaching the tropopause where the return
24 signal is significantly weaker. Figure 4 shows the effective range dependent resolution
25 obtained using the algorithm developed by Leblanc et al., 2016b. The left y-axis shows the
26 effective resolution during SCOOP in meters above sea level that was applied to the
27 AMOLITE ozone data in Figure 5. Figure 5a represents a 30-minute average of the LIDAR
28 data starting from the time of the sonde launch at 401 UTC on 10 August 2016 and Figure 5b
29 is also a 30-minute average at 2103 UTC on 16 August 2016. These two profiles were shown
30 to represent the typical results contrasting the range of the ozone DIAL during nighttime and
31 daytime operation. Typically, the DIAL measurements during the nighttime will reach a
32 range of over 10 km above ground level and dip to 7 km above ground level during high solar



1 background. The agreement between AMOLITE and the ozone sonde on both days is very
2 good, with the LIDAR staying within approximately 10% of the ozone sonde values and no
3 obvious bias throughout the profile. Note the sonde data is plotted at the highest vertical
4 resolution available. It is also important to note that the geophysical separation of the sonde
5 at altitudes of 12 km above sea level is 20-30 km for these cases, which can easily account for
6 the larger differences between the sonde and LIDAR as the altitude increases. On some days
7 during the study the LIDAR/sonde agreement varied significantly, particularly at the higher
8 altitudes, due to the large geophysical separation of the two measurements. This can be
9 shown in Figure 6 which represents the average of all 14 LIDAR/sonde comparisons. The
10 middle panel clearly shows that up to 8 km the lidar agrees to within 5% of the sonde, with
11 larger differences aloft where there are fewer number of coincidences and the geophysical
12 separation with the sonde increases.

13 The entire SCOOP campaign is captured in the false color ozone DIAL plot shown in Figure
14 7. AMOLITE was the only fully autonomous LIDAR operating during SCOOP. The
15 advantages of a fully autonomous LIDAR system are easily recognized in its ability to capture
16 a continuous dataset throughout the complete daylight cycle while capturing the dynamics and
17 mixing of long term events. The ozone DIAL is reaching the lower stratosphere, enabling
18 observations of STT events. The signal to noise was affected 11-14 August when there was
19 an air conditioner failure. The outside temperature was reaching over 30 C and the single
20 remaining air conditioner was unable to keep up with the cooling demand of two LIDARs
21 operating simultaneously. A decision was made to turn off the aerosol/water vapor LIDAR
22 for the remainder of the study to focus on the ozone inter-comparison.

23 The two plots in Figure 8 show the advantage of coincident measurements of ozone and water
24 vapor. In this case a stratospheric intrusion which starts just after 1200 UTC on 10 August,
25 mixes down to approximately 4 km above sea level and persists for over three days. The
26 water vapor plot (see Figure 8b), even though it represents night time measurements only,
27 clearly shows the very dry air coincident with the high ozone concentrations of the
28 stratospheric intrusion. The water vapor values below 4 km are also very interesting. Initially
29 on 10 August there also appears to be very dry air (and high ozone values) which may also
30 represent a prior stratospheric intrusion, followed by a more defined boundary layer with an
31 increase in water vapor, more typical of boundary layer air. The water vapor channel was
32 calibrated as described by Al Basheer et al., 2015.



1

2 **3.5 AMOLITE Algorithm Validation**

3 When undergoing a system validation, it is important to not only compare the final ozone
4 profiles between DIAL systems, but determine whether the differences are instrumental
5 and/or algorithm dependent. As a result, AMOLITE's ozone algorithm was tested against a
6 standardized algorithm developed for the SCOOP validation campaign. The first step
7 required a data importer to be written that could read the simulated data into the AMOLITE
8 algorithm. The simulated data included both the simulated LIDAR data and simulated sonde
9 profiles. Next a boxcar smoothing that is applied to the AMOLITE data was turned off as
10 there is no equivalent in the standardized algorithm. The algorithm testing began by turning
11 off the dead-time correction (saturation), background correction, Savitzky-Golay smoothing,
12 Rayleigh extinction correction and variable ozone absorption cross sections (constant values
13 were used for both wavelengths), leaving only the bare bones ozone calculation. The concept
14 was to use the simulated input in both the AMOLITE and standardized algorithms, comparing
15 the results to the original simulated ozone profile with each algorithm. With all of the above
16 corrections turned off the results matched perfectly after ensuring all unit conversions were
17 done correctly and verified both algorithms were using the same resolution functions. The
18 next test involved using a different simulated ozone profile with saturation turned on.
19 Comparing this to both algorithms with dead-time correction set to 4 ns gave confidence that
20 the algorithms were both handling the saturation effects correctly. The next test involved
21 turning off all the correction terms except the Rayleigh extinction correction and testing this
22 new simulated ozone product against both the algorithms. Once it was established that both
23 algorithms were calculating the Rayleigh profile from the simulated sonde input, the output
24 matched with less than a 0.05% bias, acceptable and not unexpected from math rounding
25 errors. Proceeding to the next test, all corrections turned off, but the variable ozone
26 absorption cross sections. Here it was important to make sure the wavelengths of the system
27 were taken to sufficient accuracy to minimize errors in the values picked from the
28 standardized look-up table. In our case the wavelength values were set to the AMOLITE
29 DIAL wavelengths of 287.20 nm and 299.14 nm. Once again with a successful outcome the
30 final test was to turn on random (Poisson) noise and added sky background to the simulated
31 ozone profile. For this final test all the corrections were turned off except the background
32 correction and a second-order Savitzky-Golay convolution applied yielding a final result



1 within 0.2%. The end result of this testing gave us confidence that the AMOLITE ozone
2 algorithm was performing flawlessly. Details of the results and comparisons to the other
3 TOLNet LIDAR systems will be presented in the SCOOP validation paper (manuscript in
4 preparation).

5

6 **3.6 AMOLITE Ozone Uncertainty**

7 An uncertainty in the ozone concentration from AMOLITE can be calculated mathematically
8 for several components. For consistency with other DIAL systems within TOLNet, the
9 uncertainty calculation was based on the paper by Leblanc et al., 2016a. For a detailed
10 description of the mathematical formulations please refer to that paper. In brief, the total
11 uncertainty determined for AMOLITE (eg. See Figures 5 and 6) was based on six different
12 components: uncertainty due to detector noise, uncertainty due to saturation, uncertainty due
13 to the Rayleigh cross-section, uncertainty due to the background calculation, uncertainty due
14 to the ozone cross-section, and uncertainty due to the air number density. To calculate these
15 uncertainties, one must also make estimates of dead time error (estimate 10%), the Rayleigh
16 error (estimate 1%), the sonde pressure uncertainty (estimate 20 Pa) and the temperature
17 uncertainty (estimate 0.3K). The AMOLITE uncertainty calculations, for each individual
18 uncertainty, successfully compared to the standardized algorithm uncertainty for a test profile.
19 The altitude at which the AMOLITE ozone profiles get truncated is based on a total
20 uncertainty threshold value chosen to be 15 % based on AMOLITE/sonde comparisons.

21

22 **4 AMOLITE: Oski-ôtin Measurements**

23 After the SCOOP campaign, AMOLITE was transported back to ECCC's Centre For
24 Atmospheric Research Experiments where the air conditioning unit was repaired and routine
25 maintenance was done on the instrument to prepare it for deployment to the oil sands region in
26 northern Alberta. AMOLITE started collecting the full suite of data products on 3 November
27 2016. The instrument has run fully autonomous, collecting a year's worth of consecutive data
28 except for a couple of weeks in July when the instrument was down for a service visit due to a
29 laser failure, and two shorter periods of time for routine maintenance requirements. During
30 the first year of operation, the autonomous ozone, aerosol and water vapor LIDAR
31 measurements provided a near continuous dataset, observing many atmospheric processes and



1 transport over a range of scales and altitudes. The following sections give examples of three
2 selected periods throughout the year showing the impact of long-range transport events,
3 atmospheric dynamics and local industrial sources as well as seasonal variability.

4 **4.1 6-13 November 2016**

5 Stratospheric intrusions were frequently observed throughout the year, with sometimes three
6 or four occurrences per week. In recent years, there has been more understanding about the
7 mechanism that enables these STT events (Langford et al., 2018). However, there is still very
8 little data on the frequency and magnitude of these events and their impact on the
9 tropospheric ozone budget. For example, Figure 9 shows three false-color plots of ozone,
10 water vapor and aerosol backscatter ratio for the bottom 10 km of the atmosphere from 6-13
11 November 2016. During this week-long period two stratospheric intrusions are observed (and
12 evidence that a third is starting on the 13 November). The white areas on the ozone plot,
13 represent cloudy regions where the DIAL system is unable to retrieve ozone values. These
14 white areas correlate very well with the cloud regions displayed in the aerosol backscatter
15 ratio plot. The water vapor plot shows dry air coincident with the higher ozone
16 concentrations of the stratospheric air reaching down into the moist regions more typical of
17 the lower atmosphere. During most of the stratospheric intrusions over the Oski-ötín site, it
18 was noted that although the free tropospheric ozone levels were increased significantly, the
19 ozone intrusion does not always penetrate the boundary layer and increase surface values.

20 A series of ozone vertical profiles during the stratospheric intrusion between 9-11 November
21 is plotted in Figure 10. This plot shows the ozone concentration before the intrusion (red line)
22 where the typical background value of approximately 30 ppbv is present in the lowest 4 km.
23 As time progresses, one can clearly see the high ozone concentration, reaching 120 ppbv,
24 from the stratospheric exchange descending down to lower and lower altitudes. The impact
25 increased the tropospheric budget by almost a factor of 2. Figure 11 shows only the lowest 4
26 km of the ozone plot compared to the ground level observations of ozone and NO_x. Visually
27 there is reasonably good agreement between the ground level measurements at the DIAL
28 measurements around 600m (the lowest few LIDAR bins can be unreliable as they are
29 strongly dependent on the alignment and temperature fluctuations inside the trailer). It is also
30 important to consider the height of the boundary layer (see Figure 12a) and the mixing of the
31 lowest water vapor region, which during the winter time can be significantly lower. The
32 ozone/NO_x relationship in Figure 11b is not the typical diurnal relationship that can be



1 observed, in part due to the stratospheric intrusion event, but also due to industrial plume
2 sources impacting the site. For several hours on 7, 8 and 9 November the ozone values
3 approach 0. There is an increase in ozone during the daytime hours (solar day is
4 approximately 1400 to 0000 UTC during this period), but also an increase during the night
5 time on 10, 11 and 12 November when the stratospheric intrusion occurred. Figure 12 shows
6 the aerosol LIDAR plot for the lowest 4 km along with various chemical and particulate
7 tracers from CAM1. The aerosol LIDAR plot gets down to approximately 100 above ground
8 level, which during the winter months is necessary to observe the boundary layer and plume
9 dynamics. There is a good correspondence between the increase in aerosol shown by the
10 LIDAR and the PM_{2.5} trace over the entire period. The increase in particle concentration is
11 linked to the presence of the plume impacting the site. As the plume impacts the ground
12 directly, there is a substantial bump in the PM_{2.5} concentration. Figures 12c and 12d also
13 indicate that the air is from an industrial source where there is high sulphate, CO₂, CO and
14 CH₄ concentrations. This is the first example where the vertical context given by the LIDAR
15 aids in the understanding of the ground-based measurements.

16

17 **4.2 29-31 August 2017**

18 Another occurrence that can change the ozone budget is forest fires. Ozone production during
19 forest fire activity is well documented and can have an impact on local air quality. During the
20 period of 29-31 August, smoke from a forest fire was advected into the region as shown in the
21 MODIS (Moderate Resolution Imaging Spectroradiometer) true color image acquired from
22 the Terra satellite on the 31 August 2017 (see Figure 13). The ozone plot shown in Figure
23 14a presents a significant amount of ozone in the free troposphere. The enhanced ozone
24 signature on 29 August is from a stratospheric intrusion whereas the enhanced ozone on 30
25 and 31 August is a result of forest fire smoke. This can be clearly seen by the large aerosol
26 burden in Figure 14b coincident with the ozone as well as the depolarization ratio plot in
27 Figure 14c, showing a value of about 5%, consistent with other smoke plume measurements.

28 A diurnal cycle of ozone is shown in Figure 15b with increased ozone due to the smoke
29 impacting the surface around 00 UTC 31 August, from what we hypothesize to be
30 enhancement from the forest fire. In Figure 15a a series of ozone traces at different altitudes
31 from the DIAL measurements are plotted against the ground ozone values. In this plot the



1 ozone aloft tracks the ground level ozone quite well until the ozone enhanced air from the
2 forest fire smoke begins to descend over the site. The noisy ozone values around the 1000m
3 level are a result of an error in ozone when the aerosol concentrations were very high (see
4 Figure 14 (a) and (b) around 1500 UTC to 1700 UTC on 31 August). There is also evidence
5 that the smoke impacted the surface from 00 UTC – 1800 UTC on August 31st shown in
6 Figure 15c-15e where an increase in H₂S, PM_{2.5} and CO also occur. Figure 16 shows an
7 overlay of the wind field from the windRASS on the LIDAR backscatter ratio plot for the
8 bottom 1 km of the atmosphere. It shows the change in wind direction around the period
9 where the smoke is impacting the ground site at Oski-ötin. There is also indications that the
10 site is being impacted by industrial sources to the south.

11 An alternative way to plot aerosol LIDAR data is to plot extinction coefficients instead of
12 backscatter coefficients. Since we are measuring the nitrogen Raman channel during the
13 night time, we can calculate the backscatter coefficient, extinction coefficient and extinction
14 to backscatter ratio also known as the S ratio. The S ratio is a useful quantity for determining
15 the air parcel type (see Strawbridge, 2013). The three-panel plot in Figure 17 shows the 355
16 nm backscatter coefficient, extinction coefficient and S ratio for 300 UTC to 1200 UTC (night
17 time) on 31 August 2017 using 10-minute average data. The near field overlap is corrected
18 and the data are plotted in kilometers above mean sea level (msl), primarily because the
19 atmospheric density obtained from sonde data is also relative to msl. The white noisy regions
20 aloft on the extreme left and right are artifacts due to the increase in sky background. The
21 backscatter coefficient plot reveals the dynamic nature of the smoke plume between 1 to 5 km
22 and a cirrus cloud layer between 8.5 to 11 km. The extinction coefficient plot is useful
23 because one can directly relate it to aerosol optical depth by integrating along the altitude
24 range. The S ratio plotted as a 10-minute average shows extraordinary detail within the
25 smoke plume with values ranging approximately 40 to 65 sr. These values are consistent
26 with the value of 45 to 65 sr reported by Barbosa et al. (2014) and are consistent with several
27 other observations provided in Table 3 of Ortiz-Amezcuca et al. (2017). Figure 17 also shows
28 the boundary layer aerosols with an S ratio of 20 to 35 sr, indicative of larger particles in the
29 moist boundary layer air (see water vapor plot in Figure 14d) and 10 to 15 sr in the cirrus
30 cloud. A more typical plot in the literature is to show a one-hour average S ratio. Figure 18
31 shows a one-hour average taken between 800 UTC and 900 UTC. For highly variable
32 conditions such as a forest fire plume, the one-hour average may result in underestimating the
33 maximum S value. It is also very difficult to measure the S value in the free troposphere



1 when there is very little aerosol present, such as this case. Those values will be very noisy
2 and have been discriminated out of the dataset shown here. Applying a night time S ratio
3 profile, particularly on features like forest fire plumes and cirrus clouds, can greatly improve
4 the daytime product over using standard look-up table S values for different air types.

5

6 **4.3 4-9 September 2017**

7 The ozone plot for 4-9 September 2017 (see Figure 19a) has several processes occurring
8 throughout the entire altitude range. There is a stratospheric intrusion on 4 September that
9 extends into 5 September (see dry air in Figure 19d). The increased ozone in the free
10 troposphere from 6-9 September is due to the forest fire activity being advected back into the
11 region. The forest fire smoke is clearly visible in the aerosol backscatter plot (see Figure 19b)
12 and the depolarization ratio plot (see Figure 19c). There is also a fairly dominant feature
13 between 800 m – 2200 m where the ozone values reach very close to 0. There are also time
14 periods where these near 0 ozone features appear to reach closer to ground level. For
15 example, around 1200 UTC on the 4-8 September, the DIAL ozone approaches 0 ppbv.
16 However, on 4 and 5 September, the very low ozone levels remain close to the ground, unlike
17 6-8 September, where the low ozone levels extend from 400m to 2000m. This is also shown
18 in Figure 20a where the ozone values from the DIAL at 500 m, 700 m and 900 m are plotted
19 against the ground level ozone. The very low surface ozone around 1200 UTC on 7
20 September remains low well up into the lower troposphere. The low ozone levels around
21 1200 UTC on 8 September is an artifact due to the very high aerosol loading. The surface
22 ozone levels (see Figure 20b) on September 4 range from a low of 10 ppbv around 1200 UTC
23 to 20 ppbv. Figure 21 shows the winds were primarily coming from the north, where there are
24 fewer industrial sources to impact the ground site. However, on 5 September the winds are
25 coming from the south where the industrial sources are impacting the site as shown by the
26 increase in NO_x (see Figure 20b), sulphates (see Figure 20c), PM_{2.5} (see Figure 20d) and CO₂
27 (see Figure 20e).

28 The ground level ozone increasing to 50 ppbv around 1800 UTC on 7 September, dropping to
29 35 ppbv around 300 UTC on 8 September is mostly due to the southerly wind (see Figure 21)
30 bringing the industrial plumes to the ground site. The DIAL ozone shows ozone levels
31 reaching 80 ppbv within 500 m of the surface. There is also an increase in SO₄ and CH₄



1 during this time period. The diurnal ozone cycle is very well established throughout this
2 entire study period, except when the elevated ozone from the forest fire smoke is mixed down
3 to the surface starting around 600 UTC on 8 September (note the increase in NO_2 , but no NO).
4 The increase in ground level ozone throughout the night time reaches values of up to 25 ppbv.
5 There is also a steep increase in $\text{PM}_{2.5}$ levels (from 25 to $50 \mu\text{g m}^{-3}$) and CO around 1500
6 UTC on 8 September coincident with the LIDAR backscatter ratio plot shown in Figure 19b
7 indicative of an increased concentration of the biomass burning plume impacting the ground
8 site. The wind has also shifted from a southerly flow to eventually a northerly flow. The
9 resultant ozone at the ground is a mixture of local chemistry and ozone rich air transported
10 into the region.

11 A plot of the backscatter coefficient, extinction coefficient and S ratio from 7-9 September
12 (see Figure 22) shows the contrast between the smoke plume on 8 September and the
13 boundary layer aerosols and industrial plume (around 2 km on 7 September). The smoke
14 plume S ratios are slightly smaller (35 to 55 sr), likely indicative of more aged smoke, see the
15 one-hour average plot between 1000 UTC and 1100 UTC shown in Figure 23c. The LIDAR
16 ratio, S, can also be calculated for 532 nm. However, there is significantly less signal-to-noise
17 so the 10-minute average false color plots were not produced. A comparison was made for a
18 one-hour average during the smoke plumes that were present on 31 August and 8 September
19 (see Figure 24a and 24b). The S ratio for 532 nm on 31 August ranges between 40 to >100 sr
20 while on 8 September ranges between 40 to 70 sr. These values are consistent with the higher
21 532 nm S ratio values reported in Table 3 of Ortiz-Amezcu et al. (2017). The advantage of
22 having an S ratio at two wavelengths, is that one can now calculate the Angstrom exponent
23 (see Figure 24c and 24d). The Angstrom exponent is inversely related to the average size of
24 the particles. On 31 August the Angstrom exponent was 1.56 ± 0.2 between 2 to 4.2 km in
25 contrast to 1.35 ± 0.2 between the 2 to 4 km 8 September. These values are consistent with
26 what others have reported for biomass burning (see Table 3 by Ortiz-Amezcu et al. (2017)).
27 During this six-day period it would be very difficult to understand the ground measurements
28 without the vertical context of the LIDARs.

29

30

31



1 **5 Conclusions and future work**

2 Environment Canada has successfully designed, built and deployed a fully autonomous
3 ozone, aerosol and water vapor LIDAR system called AMOLTE. The instrument participated
4 in a validation campaign with other tropospheric ozone LIDARs where the continuous
5 operation of AMOLITE provided a unique dataset showing the complete evolution of
6 atmospheric events. The instrument underwent an extensive validation in both the hardware
7 and software algorithm processing to provide confidence in the AMOLITE ozone profiles
8 generated. A comparison with ozone sondes revealed no bias in the AMOLITE ozone profile
9 and typical difference of less than 10 % throughout the altitude range. It was also shown that
10 stratospheric intrusions can have frequent and significant impact on free tropospheric and
11 sometimes even surface measurements. In some cases the ozone concentration at the surface
12 can be increased by a factor of 2. It was also shown that higher ozone levels in forest fire
13 plumes can also impact local air quality. The lidar ratio was also calculated for the forest fire
14 plume and found to range between 35 to 65 sr at 355 nm and 40 to 100 sr at 532 nm. It was
15 also noted that over an eight-day period the S ratio decreased. The average Angstrom
16 exponent went from 1.56 on 31 August to 1.35 on 8 September. The three LIDAR system
17 provides critical information and vertical context to help interpret ground-based surface
18 measurements. The primary motivation in building AMOLITE, was to collect continuous
19 LIDAR profiles, except during precipitation, to improve our understanding of the impact and
20 extent of long-range transport and other pollution events on air quality at local, regional and
21 national scales. Developing an autonomous LIDAR facility significantly reduces the
22 operational field costs of maintaining on site personnel. The development of the instrument
23 was possible due to recent technological advancements in laser technology and internet-
24 controlled electronics. A sophisticated control program was developed to provide safe
25 operations, extensive system controls and the storage, transmission and display of the data in
26 near real-time. One of the challenges with an autonomous multi-LIDAR system is the large
27 volume of data produced. While the quick look products that are currently produced are very
28 useful to survey data quality and periods of interest in will be necessary to develop algorithms
29 to meet the data archival needs and produce various product data levels. Some of these will
30 include automated cloud screening, aerosol corrections and possibly other derived products
31 such as boundary layer height. The implementation of these algorithms in the future will
32 provide a valuable dataset for the current location as well as future observation sites.



1 Current plans are underway to add a second telescope to the ozone DIAL to allow
2 measurements closer to the surface. A couple of different designs are being investigated that
3 will fill in the gap between 100 m to 500 m. This is quite important, particularly during the
4 winter months and night time operation, when the boundary layer can often be less than 500
5 m in height.

6

7 **Acknowledgements**

8 The project was supported by the Environment and Climate Change Canada's Climate
9 Change and Air Quality Program (CCAP) and the Joint Oil Sands Monitoring program
10 (JOSM).



1 **References**

2

3 Aggarwal, M., Whiteway, J., Seabrook, J., Gray, L., Strawbridge, K., Liu, P., O'Brien, J., Li,
4 S.-M., and McLaren, R.: Airborne Lidar Measurements of Aerosol and Ozone Above the
5 Canadian Oil Sands Region, Atmos. Meas. Tech. Discuss., [https://doi.org/10.5194/amt-2017-](https://doi.org/10.5194/amt-2017-391)
6 391, in review, 2017.

7 Al-Basheer, W. and Strawbridge, K.B., Lidar vertical profiling of water vapor and aerosols in
8 the Great Lakes Region: A tool for understanding lower atmospheric dynamics, J.
9 Atmospheric Sol.-Terr. Phys., 123, 144-152, 2015. doi: 10.1016/j.jastp.2015.01.005

10 Ancellet, G., Pelon, J., Beekmann, M., Papayannis, A., and Megie, G.: Ground-based lidar
11 studies of ozone exchanges between the stratosphere and troposphere, J. Geophys. Res., 99,
12 D12, 22401-22421, 1991.

13 Ansmann, A., Riebesell, M. and Weitkamp, C.: Measurements of atmospheric aerosol
14 extinction profiles with a Raman lidar, Opt. Lett. 15, 746-748, 1990.

15 Ashmore, M. R., Assessing the future global impacts of ozone on vegetation. Plant, Cell &
16 Environment, 28: 949-964, 2005. doi:10.1111/j.1365-3040.2005.01341.x

17 Aspey, R. A., McDermid, I. S., Leblanc, T., Walsh, D. and Howe, J.: New Raman water
18 vapor and temperature lidar at JPL table mountain facility: optimization, validations and
19 sonde intercomparison, Proc. SPIE Lidar Remote Sensing Conference, Stockholm, Sweden,
20 11-14 September 2006, 63670A, 2006.

21 Baray, J.-L., Courcoux, Y., Keckhut, P., Portafaix, T., Tulet, P., Cammas, J.-P., Hauchecorne,
22 A., Godin Beekmann, S., De Mazière, M., Hermans, C., Desmet, F., Sellegri, K., Colomb, A.,
23 Ramonet, M., Sciare, J., Vuillemin, C., Hoareau, C., Dionisi, D., Dufлот, V., Vèrèmes, H.,
24 Porteneuve, J., Gabarrot, F., Gaudo, T., Metzger, J.-M., Payen, G., Leclair de Bellevue, J.,
25 Barthe, C., Posny, F., Ricaud, P., Abchiche, A., and Delmas, R.: Maïdo observatory: a new
26 high-altitude station facility at Reunion Island (21° S, 55° E) for long-term atmospheric
27 remote sensing and in situ measurements, Atmos. Meas. Tech., 6, 2865-2877,
28 <https://doi.org/10.5194/amt-6-2865-2013>, 2013.

29 Barbosa, H. M. J., Barja, B., Pauliquevis, T., Gouveia, D. A., Artaxo, P., Cirino, G. G.,
30 Santos, R. M. N., and Oliveira, A. B.: A permanent Raman lidar station in the Amazon:



- 1 description, characterization, and first results, Atmos. Meas. Tech., 7, 1745-1762,
2 <https://doi.org/10.5194/amt-7-1745-2014>, 2014.
- 3 Bock, O., Bossler, P., Bourcy, T., David, L., Goutail, F., Hoareau, C., Keckhut, P., Legain, D.,
4 Pazmino, A., Pelon, J., Pipis, K., Poujol, G., Sarkissian, A., Thom, C., Tournois, G., and
5 Tzanos, D.: Accuracy assessment of water vapour measurements from in situ and remote
6 sensing techniques during the DEMEVAP 2011 campaign at OHP, Atmos. Meas. Tech., 6,
7 2777-2802, <https://doi.org/10.5194/amt-6-2777-2013>, 2013.
- 8 Clough, S. A., Iacono, M. J. and Moncet, J. L.: Line-by-line calculation of atmospheric
9 fluxes and cooling rates: application of water vapor, J. Geophys. Res. 97, 761-785, 1992.
- 10 Ortiz-Amezcuca, P., Guerrero-Rascado, J. L., Granados-Muñoz, M. J., Benavent-Oltra, J. A.,
11 Böckmann, C., Samaras, S., Stachlewska, I. S., Janicka, Ł., Baars, H., Bohlmann, S., and
12 Alados-Arboledas, L.: Microphysical characterization of long-range transported biomass
13 burning particles from North America at three EARLINET stations, Atmos. Chem. Phys., 17,
14 5931-5946, <https://doi.org/10.5194/acp-17-5931-2017>, 2017.
- 15 Dionisi, D., Congeduti, F., Liberti, G. L. and Cardillo, F.: Calibration of a multichannel water
16 vapor Raman lidar through noncollocated operational soundings: optimization and
17 characterization of accuracy and variability, J. Atmos. Ocean. Tech. 27, 108-121, 2009.
- 18 Feingold, G., Eberhard, W. L., Veron, D. E., and Previdim M.: First measurements of the
19 Twomey indirect effect using ground-based remote sensors, Geophys. Res. Lett., 30, 1287,
20 2003.
- 21 Gaudel, A., Ancellet, G., Godin-Beekmann, S.: Analysis of 20 years of tropospheric ozone
22 vertical profiles by lidar and ECC at Observatoire de Haute Provence (OHP) at 44°N, 6.7°E,
23 Atmos. Environ., 113, 78-89, 2015. <https://doi.org/10.1016/j.atmosenv.2015.04.028>
- 24 Gaudel A, Cooper OR, Ancellet G, Barret B, Boynard A, Burrows JP, et al. . Tropospheric
25 Ozone Assessment Report: Present-day distribution and trends of tropospheric ozone relevant
26 to climate and global atmospheric chemistry model evaluation . Elem Sci Anth . 6 (1), 39,
27 2018. DOI: <http://doi.org/10.1525/elementa.291>
- 28 Godin, S., Carswell, A.I., Donovan, D.P., Claude, H., Steinbrecht, W., McDermid, I.S.,
29 McGee, T., Gross, M.R., Nakane, H., Swart, D.P.J, Bergwerff, H.B., Uchino, O., von der
30 Gathen, P. and Neuber, R.: Ozone differential absorption lidar algorithm intercomparison,
31 Appl. Opt. 38, 6225-6236, 1999.



- 1 Goldsmith, J. E. M., Blair, F. H., Bisson, S. E. and Turner, D. D.: Turn-key Raman lidar for
2 profiling atmospheric water vapor, clouds, and aerosols, *Appl. Optics*, 37, 4979-4990, 1998.
- 3 Granados-Muñoz, M. J. and Leblanc, T.: Tropospheric ozone seasonal and long-term
4 variability as seen by lidar and surface measurements at the JPL-Table Mountain Facility,
5 California, *Atmos. Chem. Phys.*, 16, 9299-9319, <https://doi.org/10.5194/acp-16-9299-2016>,
6 2016.
- 7 Grant, W. B.: Differential absorption and Raman lidar for water vapor profile measurements:
8 a review, *Opt. Eng.*, 31, 40-48, 1991.
- 9 Khaykin, S. M., Godin-Beekmann, S., Keckhut, P., Hauchecorne, A., Jumelet, J., Vernier, J.-
10 P., Bourassa, A., Degenstein, D. A., Rieger, L. A., Bingen, C., Vanhellefont, F., Robert, C.,
11 DeLand, M., and Bhartia, P. K.: Variability and evolution of the midlatitude stratospheric
12 aerosol budget from 22 years of ground-based lidar and satellite observations, *Atmos. Chem.*
13 *Phys.*, 17, 1829-1845, <https://doi.org/10.5194/acp-17-1829-2017>, 2017.
- 14 Kousha, T. and Valacchi, G.: The air quality health index and emergency department visits
15 for urticaria in Windsor, Canada, *J. Toxicol. Environ. Health*, 78 (8), 524-533, 2015.
16 <https://doi.org/10.1080/15287394.2014.991053>.
- 17 Kovalev, V. and McElroy, J.: Differential absorption lidar measurement of vertical ozone
18 profiles in the troposphere that contains aerosol layers with strong backscattering gradients: a
19 simplified version, *Appl. Opt.*, 33(36), 8393-8401, 1994.
- 20 Langford, A.O., Masters, C.D., Proffitt M.H., Hsie, E.-Y. and Tuck, A.F.: Ozone
21 measurements in a tropopause fold associated with a cut-off low system, *Geophys. Res. Lett.*,
22 23 (18), 2501-2504, 1996.
- 23 Langford, A.O., Alvarez, R.J., Brioude, J., Evan, S., Iraci, L.T., Kirgis, G., Kuang, S.,
24 Leblanc, T., Newchurch, M.J., Pierce, R.B., Senff, C.J. and Yates, E.L.: Coordinated
25 profiling of stratospheric intrusions and transported pollution by the Tropospheric Ozone
26 Lidar Network (TOLNet) and NASA Alpha Jet experiment (AJAX): Observations and
27 comparison to HYSPLIT, RAQMS, and FLEXPART, *Atmos. Environ.*, 174, 1-14, 2018.
28 <https://doi.org/10.1016/j.atmosenv.2017.11.031>
- 29 Leblanc, T., Walsh, T. D., McDermid, I. S., Toon, G. C., Blavier, J.-F., Haines, B., Read, W.
30 G., Herman, B., Fetzner, E., Sander, S., Pongetti, T., Whiteman, D. N., McGee, T. G., Twigg,
31 L., Sunnicht, G., Venable, D., Calhoun, M., Dirisu, A., Hurst, D., Jordan, A., Hall, E.,



- 1 Miloshevich, L., Vömel, H., Straub, C., Kampfer, N., Nedoluha, G. E., Gomez, R. M., Holub,
2 K., Gutman, S., Braun, J., Vanhove, T., Stiller, G., and Hauchecorne, A.: Measurements of
3 Humidity in the Atmosphere and Validation Experiments (MOHAVE)-2009: overview of
4 campaign operations and results, *Atmos. Meas. Tech.*, 4, 2579-2605,
5 <https://doi.org/10.5194/amt-4-2579-2011>, 2011.
- 6 Li, C., Martin, R. V., Boys, B. L., van Donkelaar, A., and Ruzzante, S.: Evaluation and
7 application of multi-decadal visibility data for trend analysis of atmospheric haze, *Atmos.*
8 *Chem. Phys.*, 16, 2435-2457, <https://doi.org/10.5194/acp-16-2435-2016>, 2016.
- 9 Lippmann, Morton: Health effects of tropospheric ozone, *Environ. Sci. Technol.*, 25 (12),
10 1954-1962, 1991. DOI: 10.1021/es00024a001
- 11 Malley, C. S., Heal, M. R., Mills, G., and Braban, C. F.: Trends and drivers of ozone human
12 health and vegetation impact metrics from UK EMEP supersite measurements (1990–2013),
13 *Atmos. Chem. Phys.*, 15, 4025-4042, <https://doi.org/10.5194/acp-15-4025-2015>, 2015.
- 14 McKee, David J., *Tropospheric ozone human health and agricultural impacts*: Lewis
15 Publishers, Boca Raton, FL, 1994.
- 16 Nakazato, M., Nagai, T., Sakai, T., and Hirose, Y.: Tropospheric ozone differential-
17 absorption lidar using stimulated Raman scattering in carbon dioxide, *Appl. Opt.*, 46(12),
18 2269-2279, 2007.
- 19 Pruppacher, H. R. and Klett, J. D.: *Microphysics of Clouds and Precipitation*, Kluwer
20 Academic Publishers, Dordrecht, Netherlands, 1997.
- 21 Ramanathan, V., Crutzen, P.J., Kiehl, J.T., and Rosenfeld, D.: Aerosols, climate, and the
22 hydrological cycle, *Science*, 294, 2119-2124, 2001.
- 23 Singh, A., Bloss, W. J., and Pope, F. D.: 60 years of UK visibility measurements: impact of
24 meteorology and atmospheric pollutants on visibility, *Atmos. Chem. Phys.*, 17, 2085-2101,
25 <https://doi.org/10.5194/acp-17-2085-2017>, 2017.
- 26 Sinha, A. and Harries, J. E.: Water vapor and greenhouse trapping: the role of far infrared
27 absorption, *Geophys. Res. Lett.*, 22, 2147-2150, 1995.
- 28 Strawbridge, K. B.: Developing a portable, autonomous aerosol backscatter lidar for network
29 or remote operations, *Atmos. Meas. Tech.*, 6, 801-816, [https://doi.org/10.5194/amt-6-801-](https://doi.org/10.5194/amt-6-801-2013)
30 2013, 2013.



- 1 Trickl, T., Vogelmann, H., Giehl, H., Scheel, H.-E., Sprenger, M., and Stohl, A.: How
2 stratospheric are deep stratospheric intrusions?, *Atmos. Chem. Phys.*, 14, 9941-9961,
3 <https://doi.org/10.5194/acp-14-9941-2014>, 2014.
- 4 Trickl, T., Vogelmann, H., Flentje, H., and Ries, L.: Stratospheric ozone in boreal fire plumes
5 – the 2013 smoke season over central Europe, *Atmos. Chem. Phys.*, 15, 9631-9649,
6 <https://doi.org/10.5194/acp-15-9631-2015>, 2015.
- 7 Trickl, T., Vogelmann, H., Fix, A., Schäfler, A., Wirth, M., Calpini, B., Levrat, G.,
8 Romanens, G., Apituley, A., Wilson, K. M., Begbie, R., Reichardt, J., Vömel, H., and
9 Sprenger, M.: How stratospheric are deep stratospheric intrusions? LUAMI 2008, *Atmos.*
10 *Chem. Phys.*, 16, 8791-8815, <https://doi.org/10.5194/acp-16-8791-2016>, 2016.
- 11 Twomey, S., The influence of pollution on the short wave albedo of clouds, *J. Atmos. Sci.*,
12 34, 1149–1152, 1977.
- 13 Twomey, S.: Aerosols, clouds and radiation, *Atmos. Environ.* 25A, 2435-2442, 1991.
- 14 Uno, I., Eguchi, K., Yumimoto, K., Takemura, T., Shimizu, A., Uematsu, M., Liu, Z., Wang,
15 Z., Hara, Y., and Sugimoto, N.: Asian dust transported one full circuit around the globe, *Nat.*
16 *Geosci.*, 2, 557-560, 2009.
- 17 Wandinger, U.: Introduction to lidar, in *Lidar -Range-resolved optical remote sensing of the*
18 *atmosphere*, C. Weitkamp (Ed.), Springer, New York, 2005.
- 19 Whiteman, D.N., Melfi, S.H. and Ferrare, R.A.: Raman lidar system for the measurement of
20 water vapor and aerosols in the Earth's atmosphere, *Appl. Opt.* 31, 3068-3082, 1992.
- 21 Whiteman, D. N.: Examination of the traditional Raman lidar technique II. Evaluating the
22 ratios for water vapor and aerosols, *Appl. Opt.*, 42, 2593-2608, 2003.
- 23 Yamamoto, G., Tanaka, M. and Kamitani, K.: Radiative transfer in water clouds in the 10-
24 micron window region, *J. Atmos. Sci.* 23, 305-313, 1966.
- 25



- 1 List of Figures:
- 2
- 3 Figure 1. (a) A picture showing AMOLITE on location during the SCOOP campaign at
- 4 Table Mountain in California. (b) A schematic diagram of the dual laser, dual LIDAR design
- 5 of AMOLITE. Both LIDAR systems are mounted on the same optical bench.
- 6 Figure 2. A schematic showing the transmitter and receiver of the aerosol and water vapor
- 7 LIDAR. A detailed optical breakout is shown for the seven-channel detector package.
- 8 Figure 3. A schematic showing the transmitter and receiver design for the DIAL ozone
- 9 system. Note the translation stage that can be moved to change which laser is used.
- 10 Figure 4. A plot showing the effective resolution of the DIAL ozone profiles. The MSL
- 11 scale was used during the SCOOP campaign and the AGL scale was used for the Oski-ôtin
- 12 data.
- 13 Figure 5. Three-panel plots showing AMOLITE ozone profile against the sonde profile, the
- 14 percentage difference between the two profiles and the horizontal sonde distance from the
- 15 launch site for (a) 2103 UTC on 10 August and (b) 401 UTC on 16 August.
- 16 Figure 6. Three-panel plot showing the average of all AMOLITE and coincident sonde
- 17 profiles throughout the entire SCOOP campaign. The number of coincident measurements
- 18 varies with altitude primarily due to the reduced altitude capability of the AMOLITE during
- 19 daytime operation.
- 20 Figure 7. False color plot of ozone from AMOLITE during the entire SCOOP campaign. The
- 21 white areas represent where no ozone data is available due to cloud and daytime background.
- 22 Figure 8. False color plots showing (a) ozone and (b) water vapor for the same time period of
- 23 10-14 August 2016.
- 24 Figure 9. False color plots the first 10 km of the atmosphere for (a) ozone (b) water vapor and
- 25 (c) aerosol backscatter ratio for the period of 6-13 November 2016 at the Oski-ôtin ground
- 26 site.
- 27 Figure 10. A plot showing ozone profiles between 9 November and 11 November as the
- 28 ozone rich stratospheric air is mixed down into the troposphere.



- 1 Figure 11. (a) False color plot showing of DIAL ozone from AMOLITE between 6-13
2 November and (b) surface measurements of ozone and NO_x during the same time period.
- 3 Figure 12. (a) False color plot of aerosol backscatter ratio for the same altitude and time
4 period as Figure 11a. CAM1 surface measurements during the same time period for (b)
5 PM_{2.5} (c) sulphates and (d) CH₄, CO, CO₂ and NO.
- 6 Figure 13. Terra MODIS true color composite image on 31 August 2017. Note the location
7 of the ground site.
- 8 Figure 14. False color LIDAR plots for 29-31 August for (a) ozone (b) backscatter ratio, (c)
9 depolarization ratio and (d) water vapor (night time only).
- 10 Figure 15. (a) DIAL ozone traces at different altitudes compared to surface ozone for the
11 same period as Figure 14. CAM1 surface measurements for same time period of (b) ozone
12 and NO_x (c) PM_{2.5} (d) sulphates and (e) CH₄, CO, CO₂ and NO.
- 13 Figure 16. WindRASS data overlaid on 29-31 August AMOLITE aerosol backscatter ratio
14 plot.
- 15 Figure 17. Three-panel plot showing the backscatter coefficient (scale = 0 to 20), extinction
16 coefficient (scale = 0 to 1) and S ratio (scale = 1 to 100) for 31 August. Only one color bar
17 scale was shown for simplicity.
- 18 Figure 18. One-hour average between 800 UTC and 900 UTC on 31 August for (a)
19 backscatter coefficient (b) extinction coefficient (c) S ratio (d) effective resolution.
- 20 Figure 19. False color LIDAR plots for 4 – 9 September for (a) ozone (b) backscatter ratio,
21 (c) depolarization ratio and (d) water vapor (night time only).
- 22 Figure 20. (a) DIAL ozone traces at different altitudes compared to surface ozone for the
23 same period as Figure 19. CAM1 surface measurements for same time period of (b) ozone
24 and NO_x (c) PM_{2.5} (d) sulphates and (e) CH₄, CO, CO₂ and NO.
- 25 Figure 21. WindRASS data overlaid on 4-9 September AMOLITE aerosol backscatter ratio
26 plot.
- 27 Figure 22. False color plots of 4-9 September for (a) backscatter coefficient (scale = 0 to 40),
28 (b) extinction coefficient (scale = 0 to 2) and (c) S ratio (scale = 1 to 100).



1 Figure 23. One-hour average between 1000 UTC and 1100 UTC on 8 September for (a)
2 backscatter coefficient (b) extinction coefficient and (c) S ratio. The effective resolution is
3 the same as Figure 18.

4 Figure 24. (a) S ratio plot of 355 nm and 532 nm for 31 August (b) S ratio plot of 355 nm
5 and 532 nm for 8 September (c) Angstrom exponent for 31 August and (d) Angstrom
6 exponent for 8 September. Same one-hour averages as Figures 18 and 23.

7

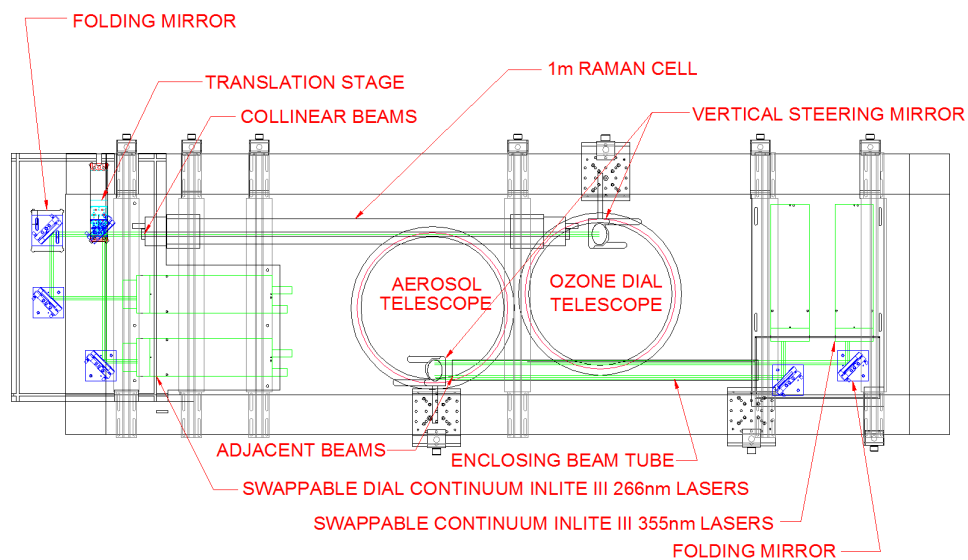


1 Fig. 1 (a)



2

3 (b)



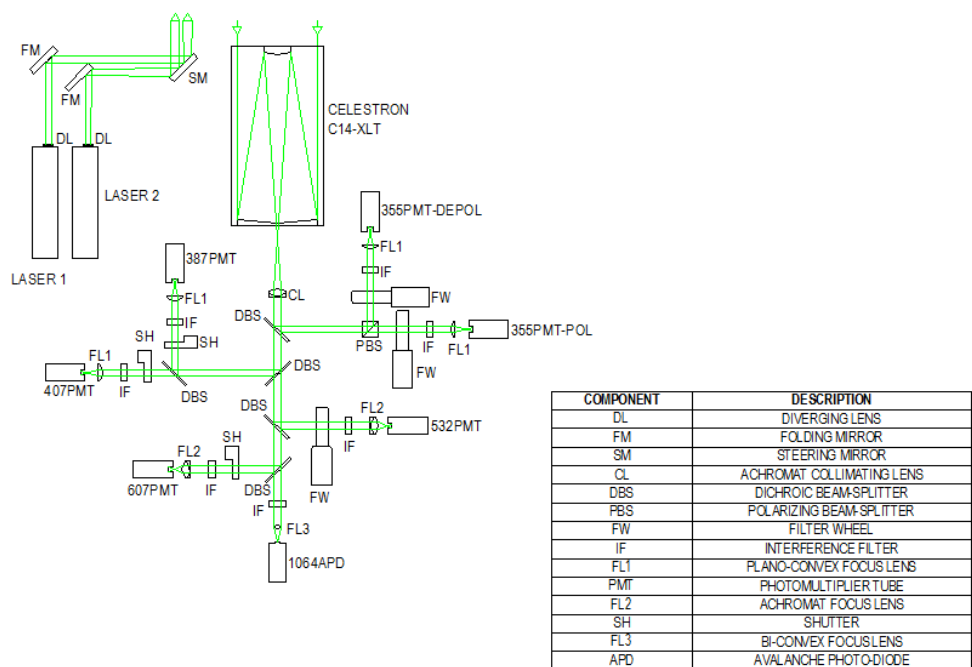
4

5



1 Fig. 2

2

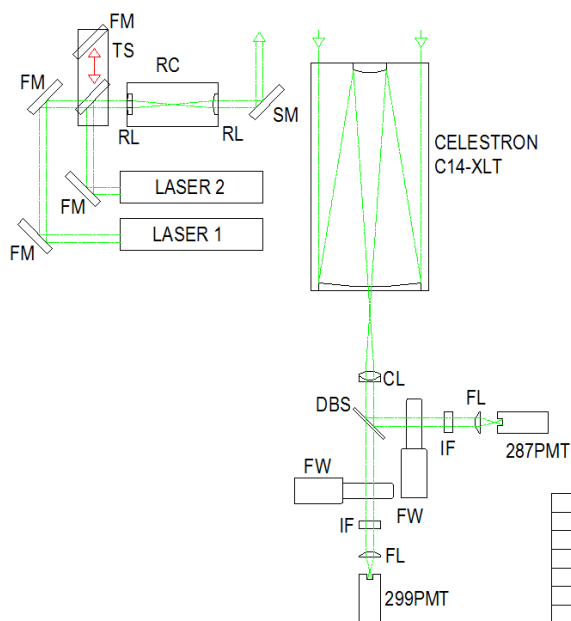


3



1 Fig. 3

2



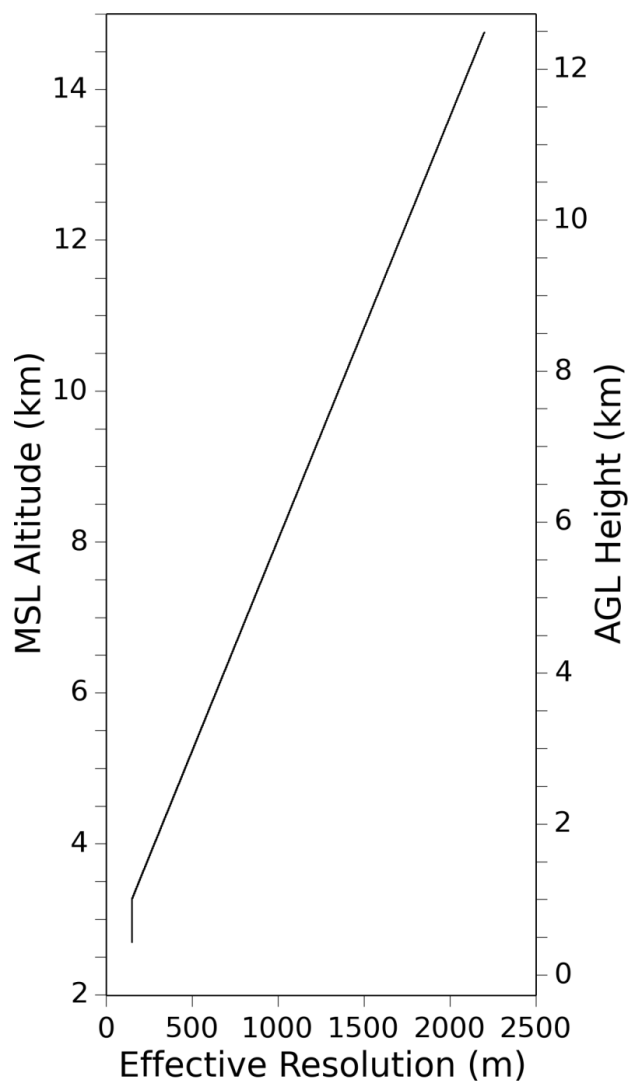
COMPONENT	DESCRIPTION
FM	FOLDING MIRROR
TS	TRANSLATION STAGE
RC	RAMAN CELL
RL	PLANO-CONVEX RAMAN LENS
SM	STEERING MIRROR
CL	ACHROMAT COLLIMATING LENS
DBS	DICHROIC BEAM-SPLITTER
FW	FILTER WHEEL
IF	INTERFERENCE FILTER
FL	PLANO-CONVEX FOCUS LENS
PMT	PHOTOMULTIPLIER TUBE

3

4



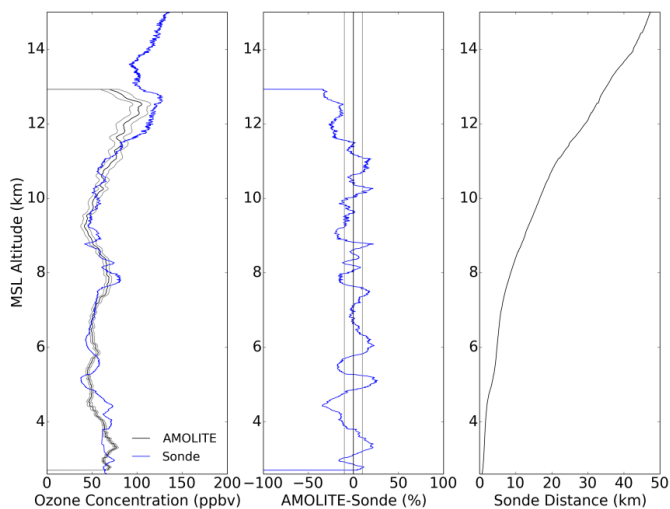
1 Fig. 4



2

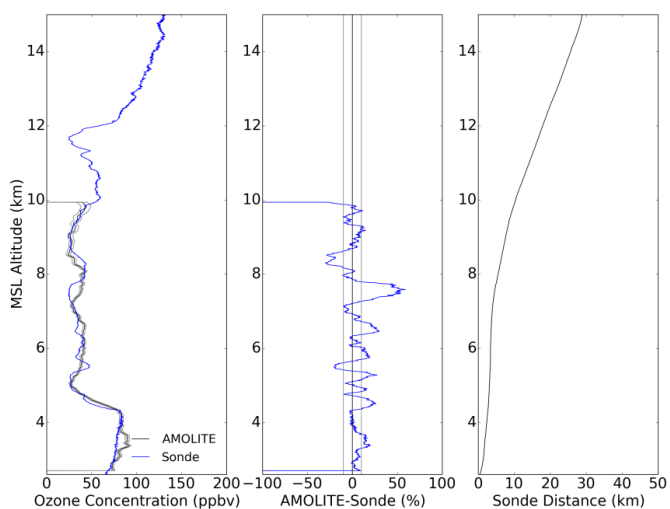


1 Fig. 5 (a)



2

3 (b)

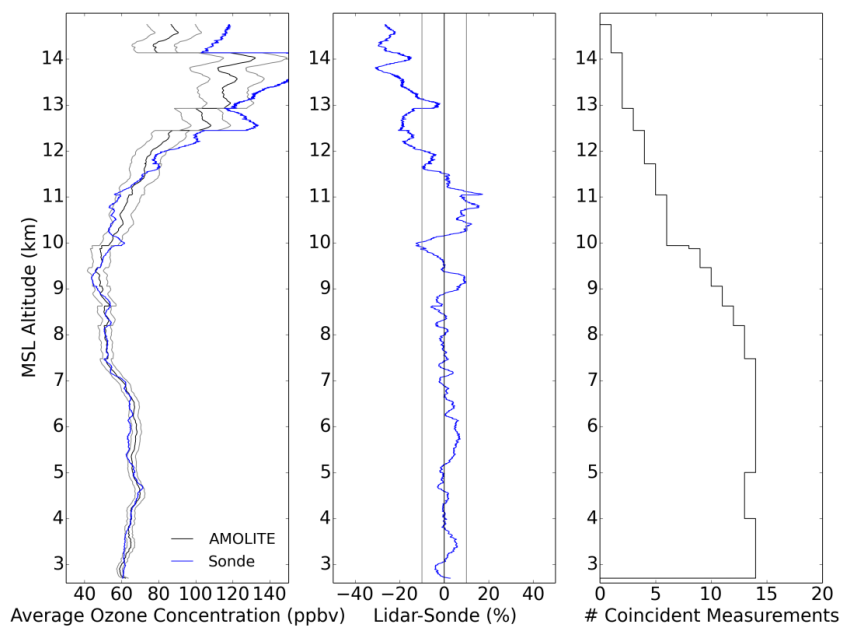


4



1 Fig. 6

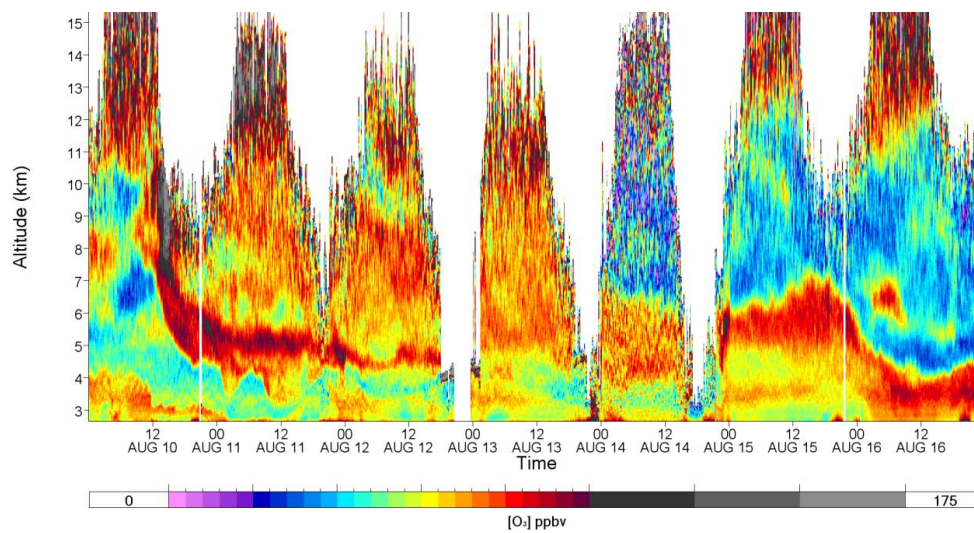
2



3



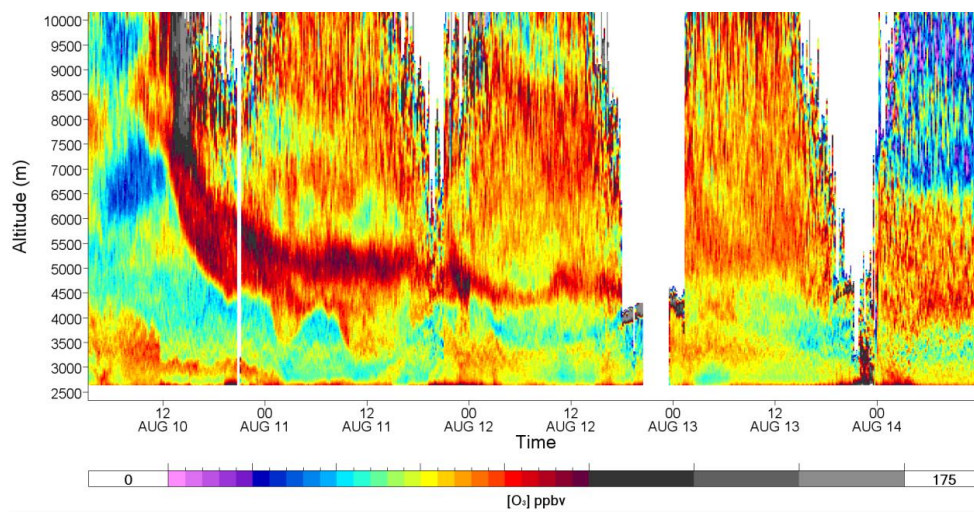
1 Fig. 7



2
3

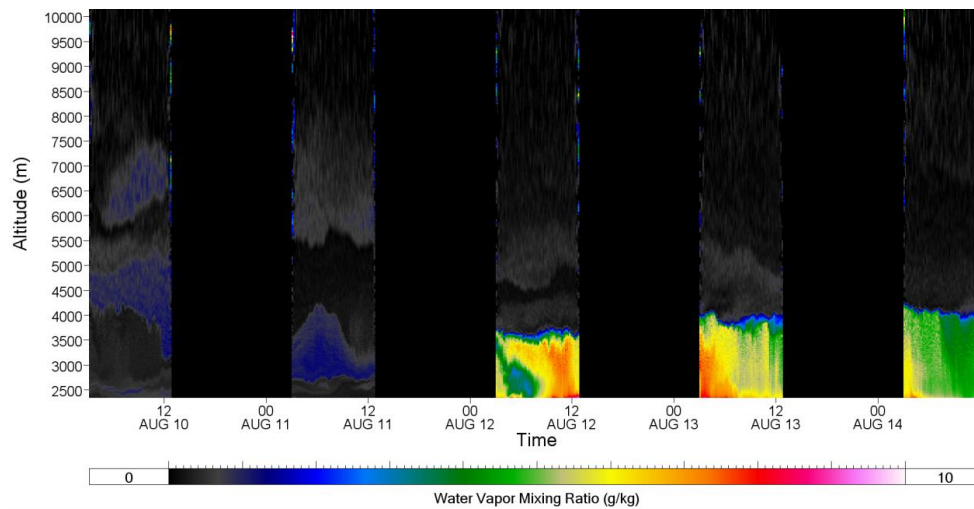


1 Fig. 8 (a)



2

3 (b)

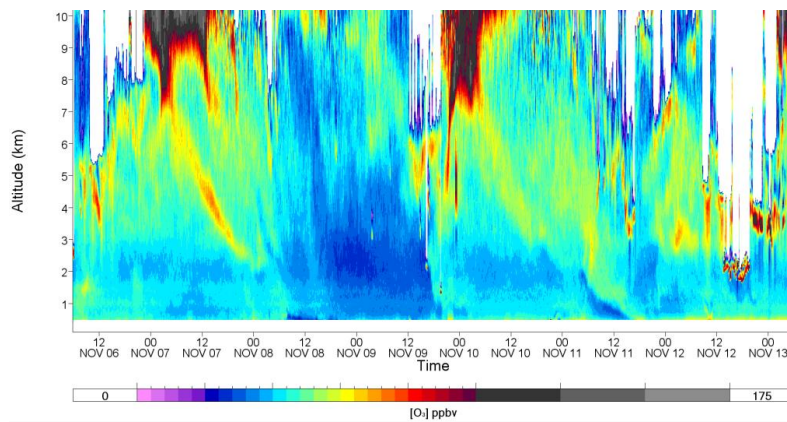


4

5

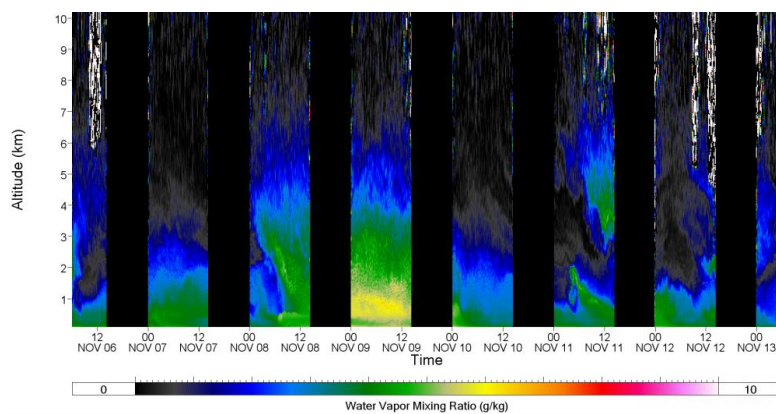


1 Fig. 9 (a)



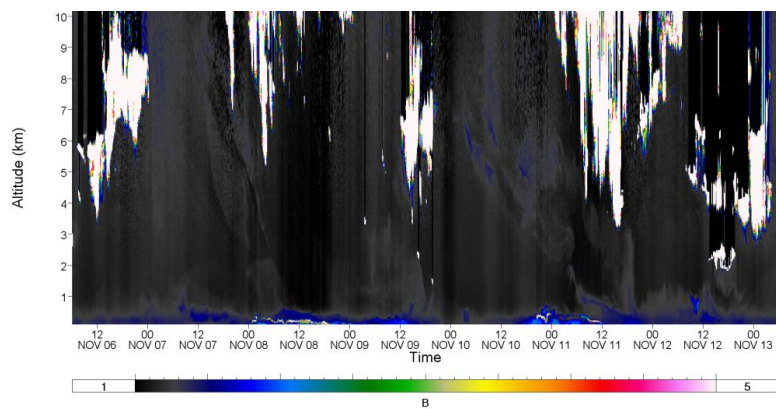
2

3 (b)



4

5 (c)

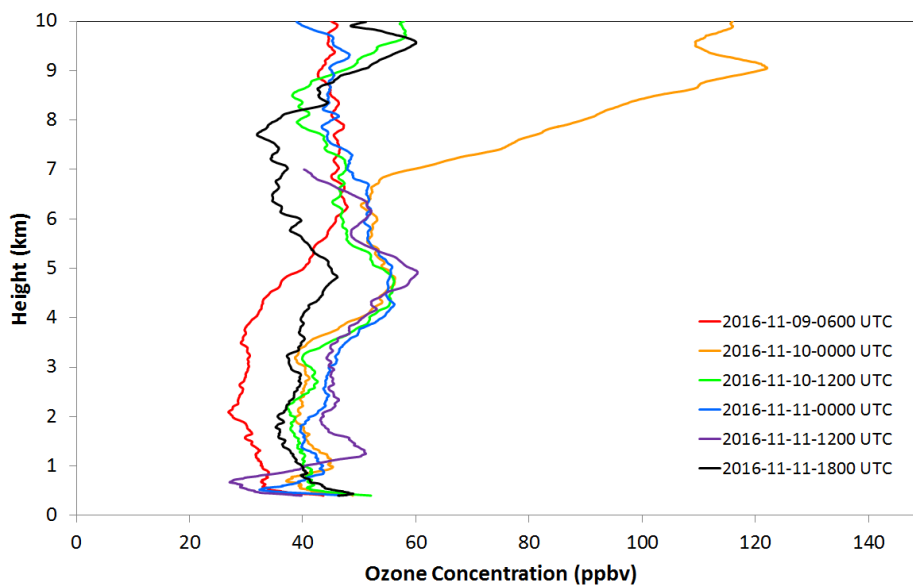


6

7



1 Fig. 10

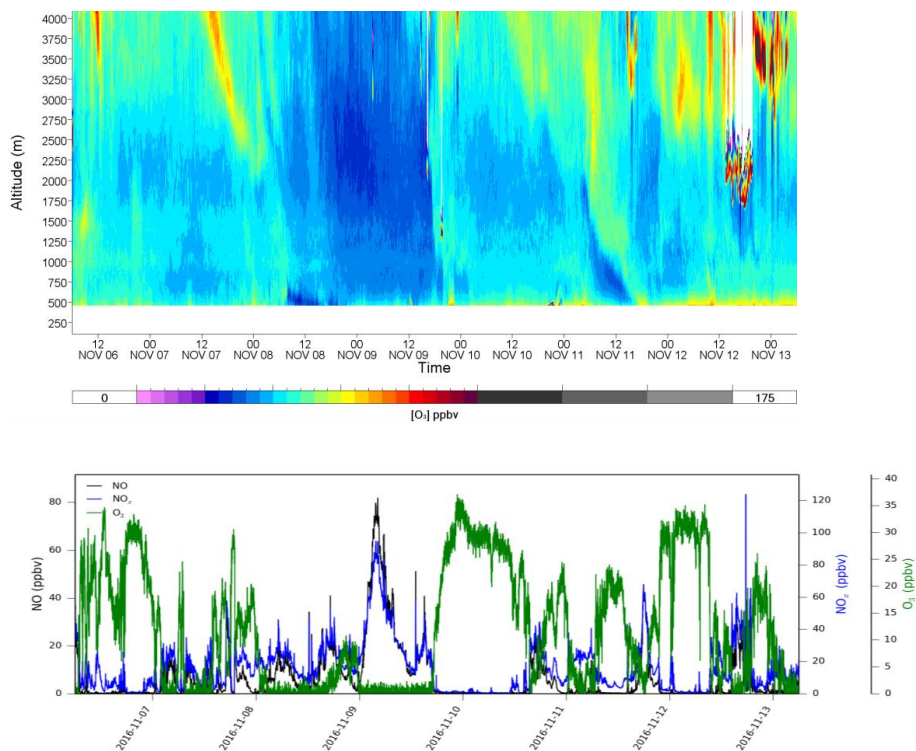


2

3

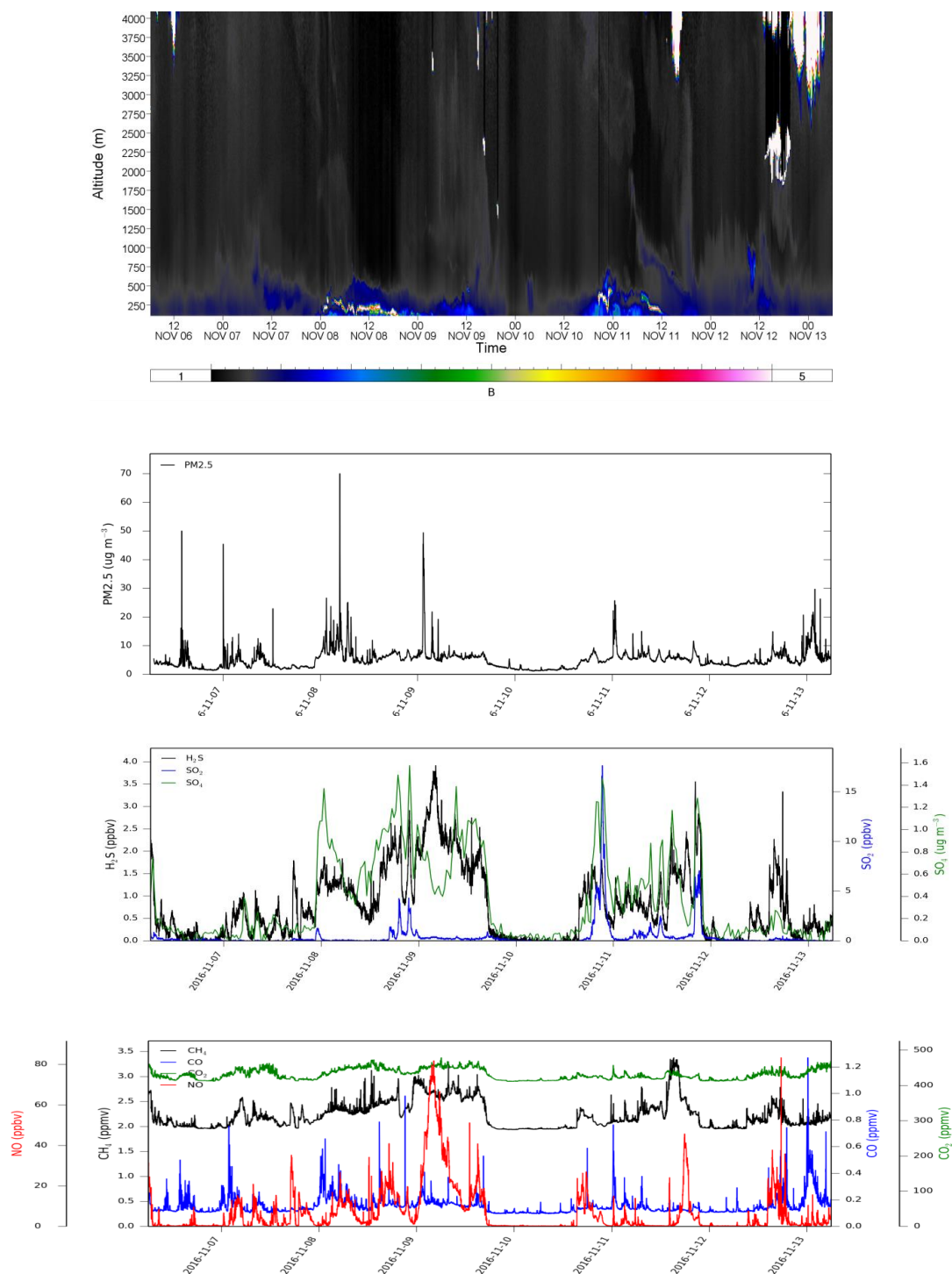


1 Fig. 11 (a)





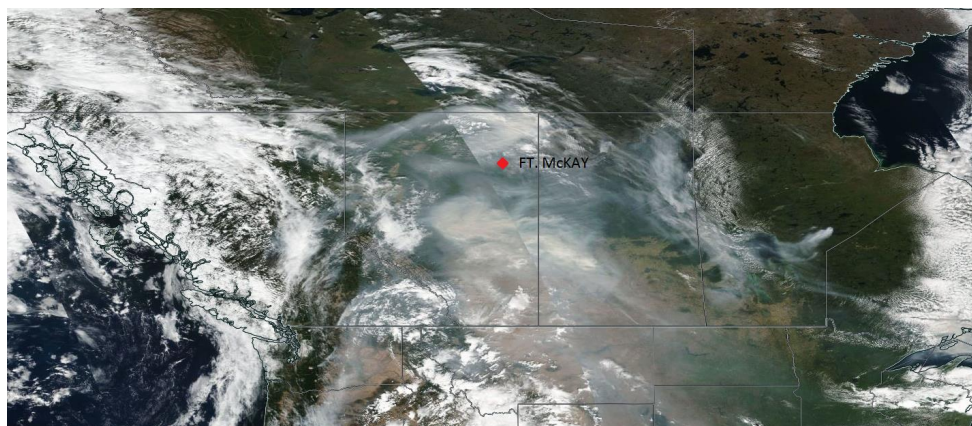
1 Fig. 12 (a)





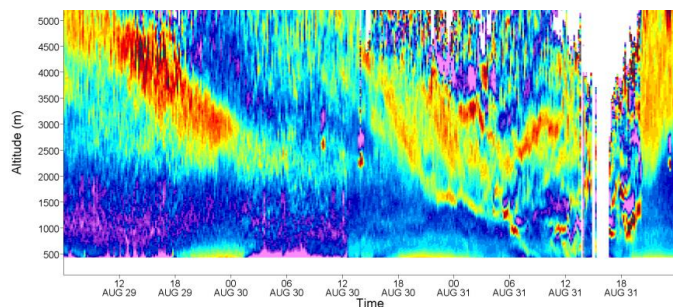
1 Fig. 13

2

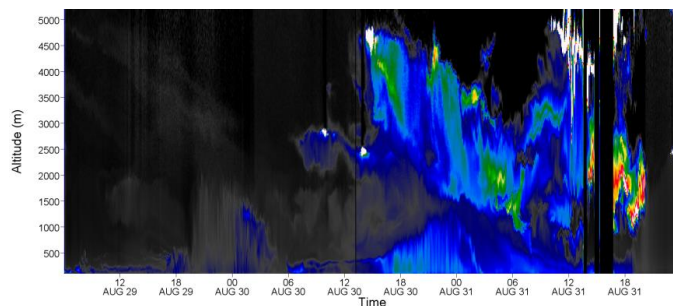




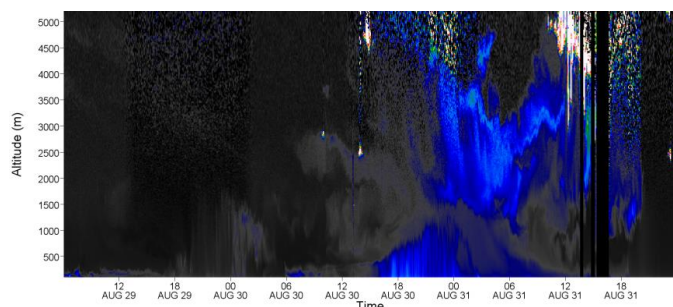
1 Fig. 14



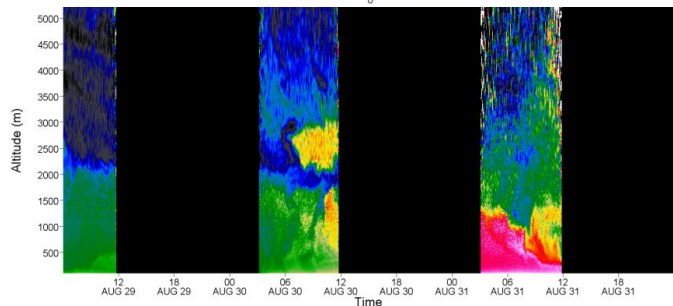
2



3



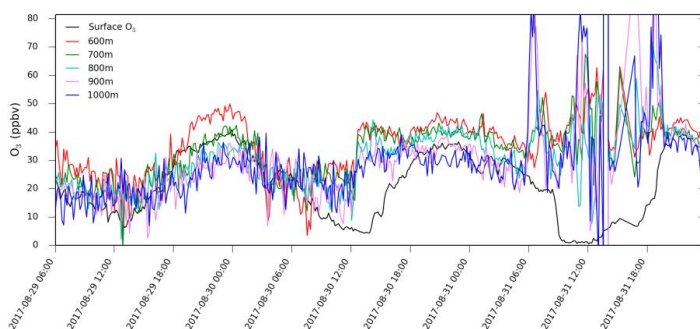
4



5

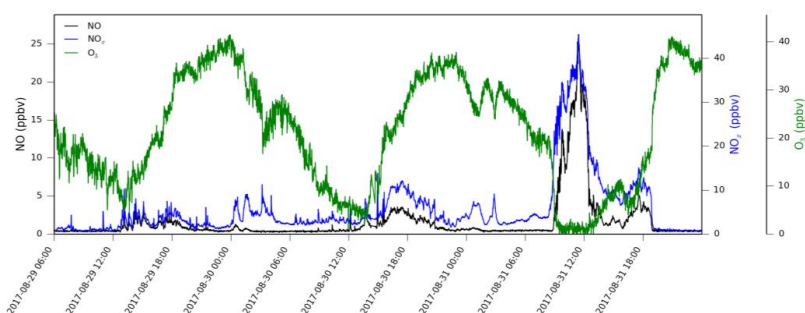


1 Fig. 15 (a)



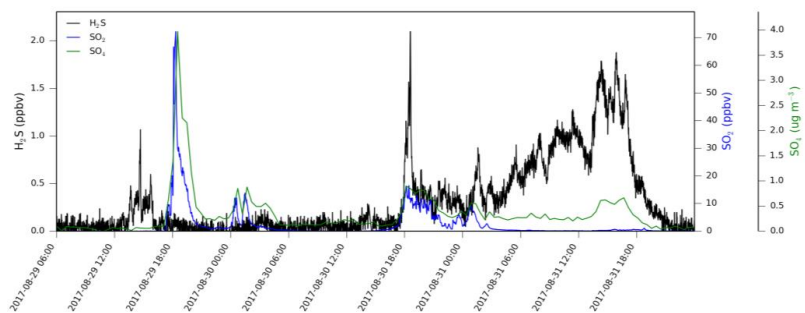
2

3 (b)



4

5 (c)

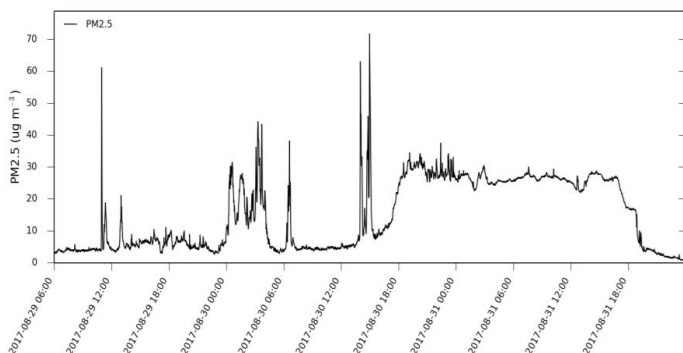


6

7

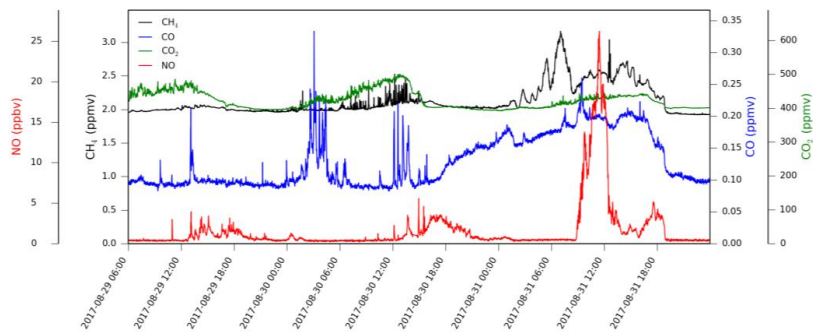
8

9 (d)



1

2 (e)



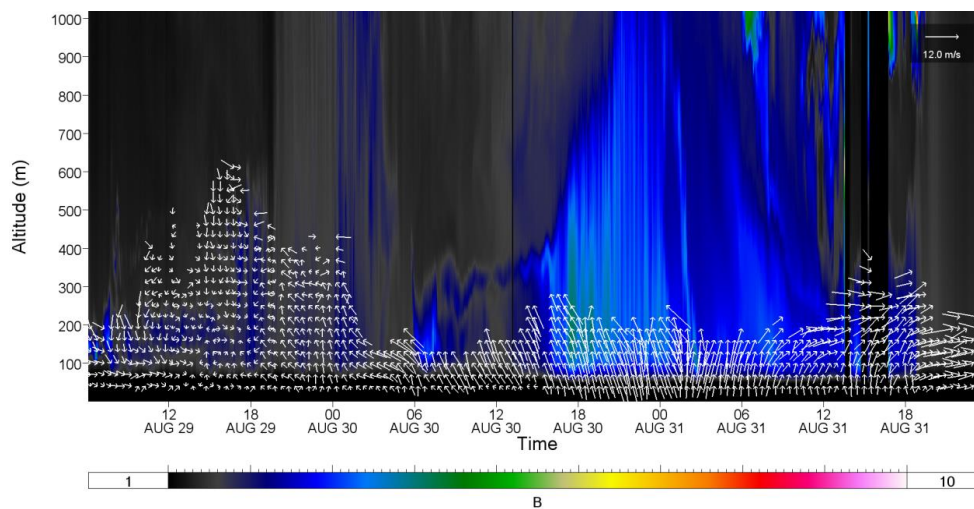
3

4



1 Fig. 16

2



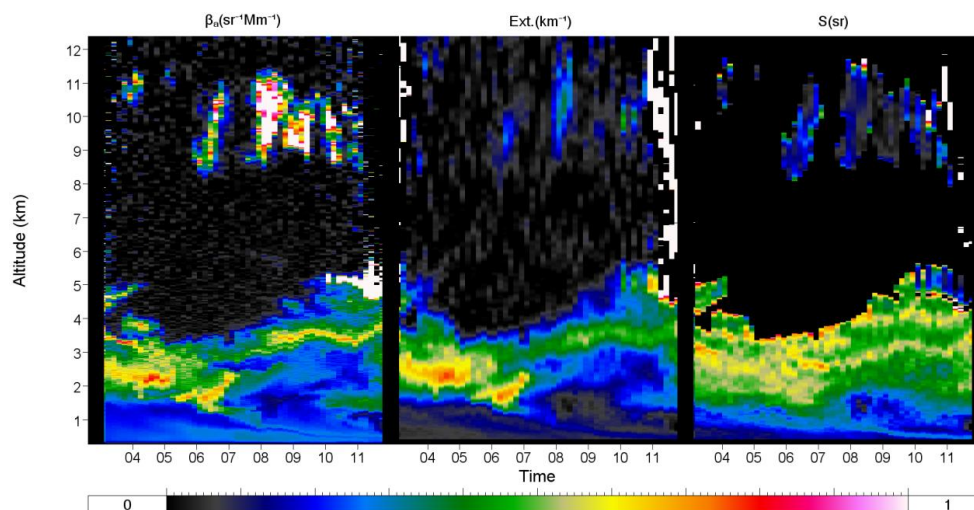
3

4

5



1 Fig. 17



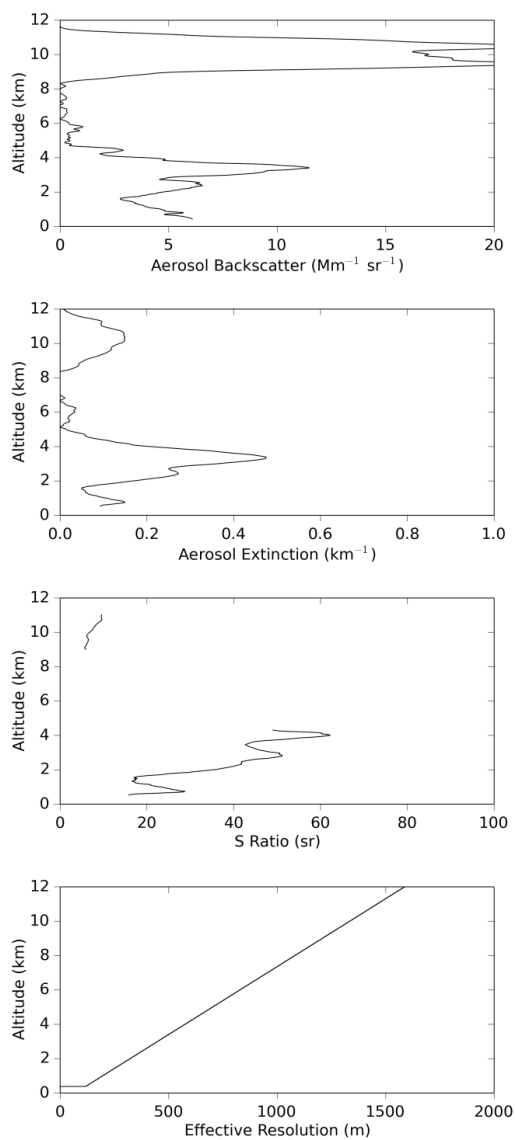
2

3

4



1 Fig. 18

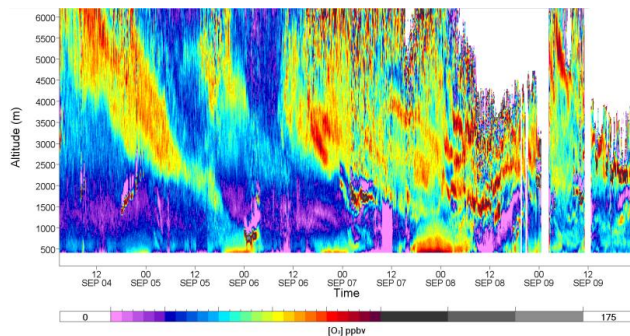


2

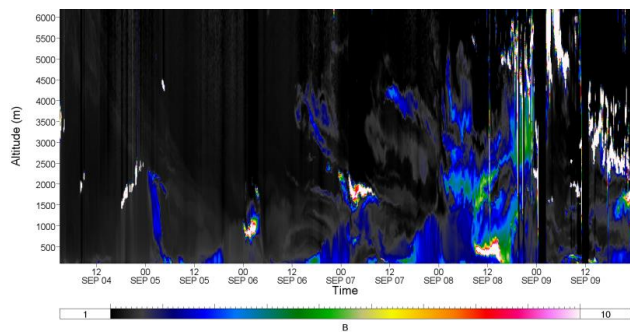
3



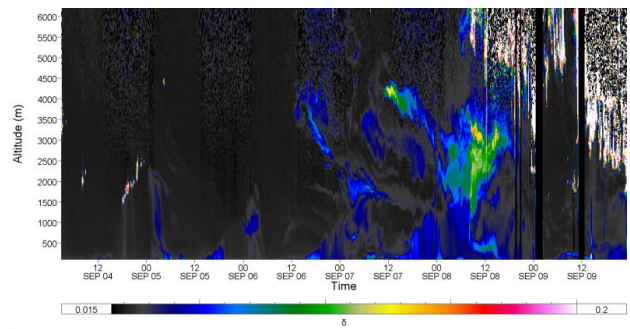
1 Fig. 19



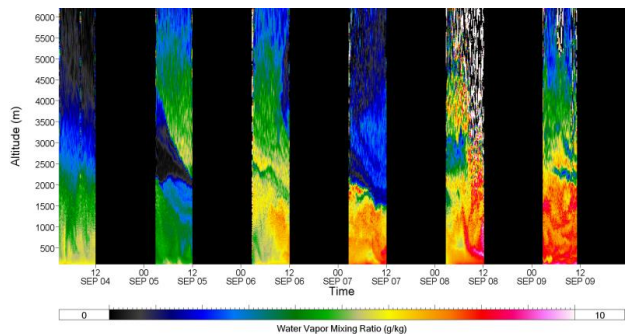
2



3



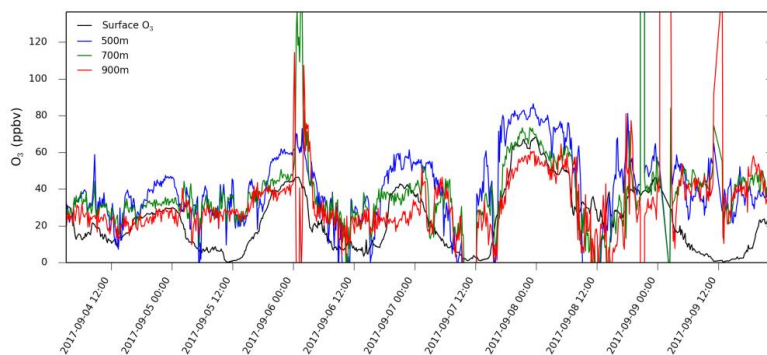
4



5

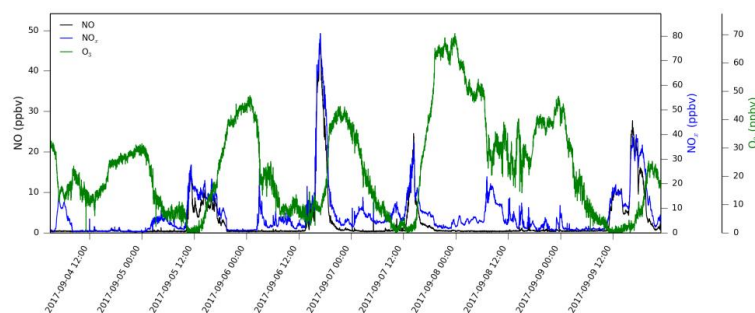


1 Fig. 20 (a)



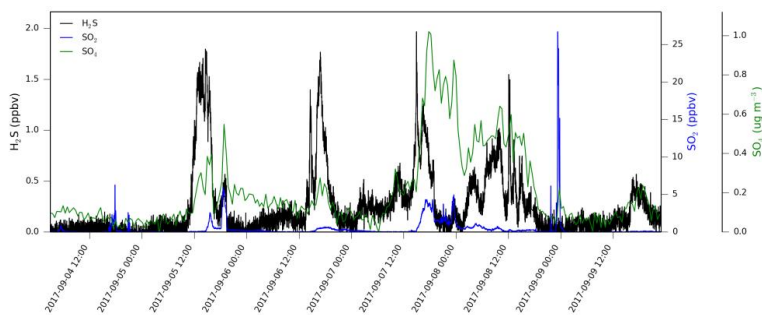
2

3 (b)



4

5 (c)

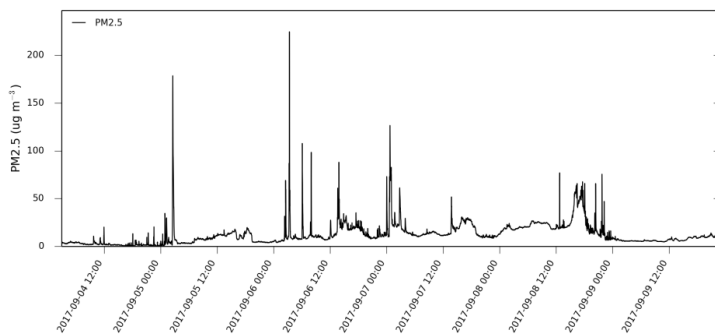


6



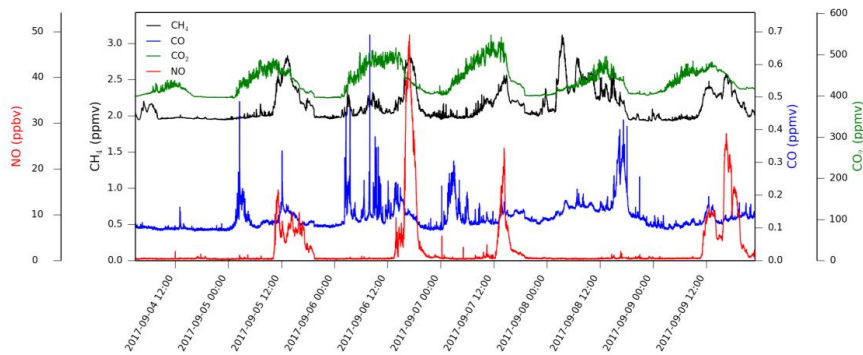
1

2 (d)



3

4 (e)

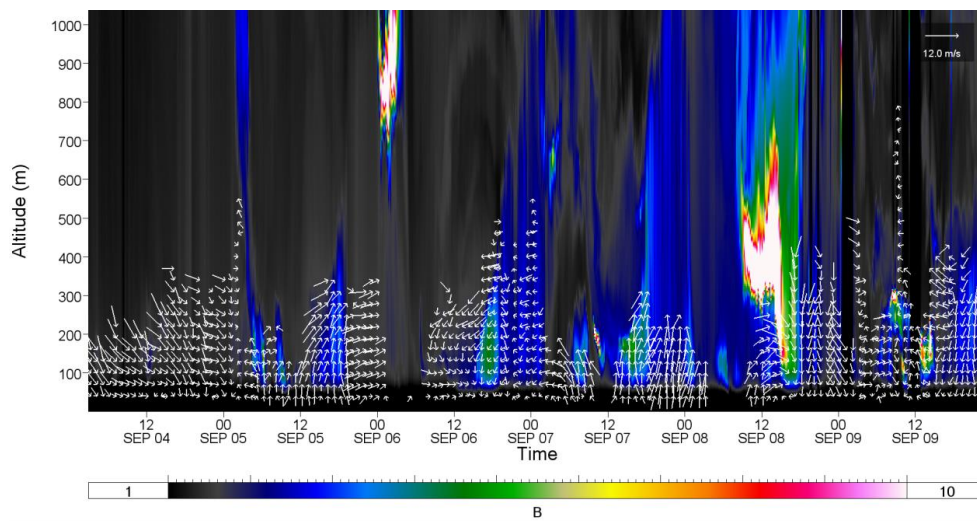


5



1 Fig. 21

2

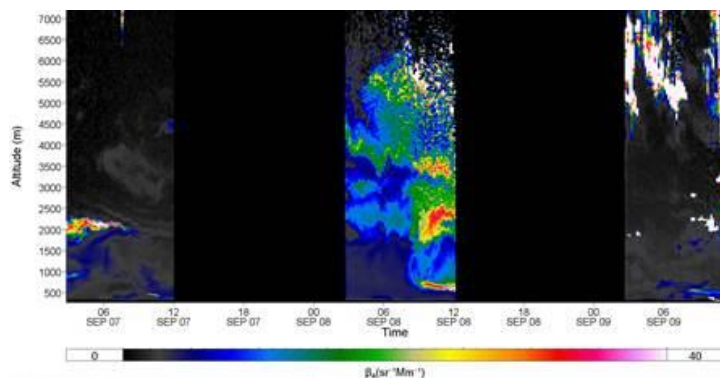


3

4

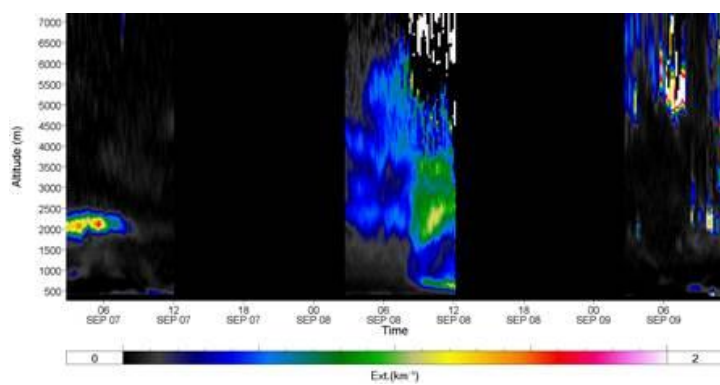


1 Fig. 22

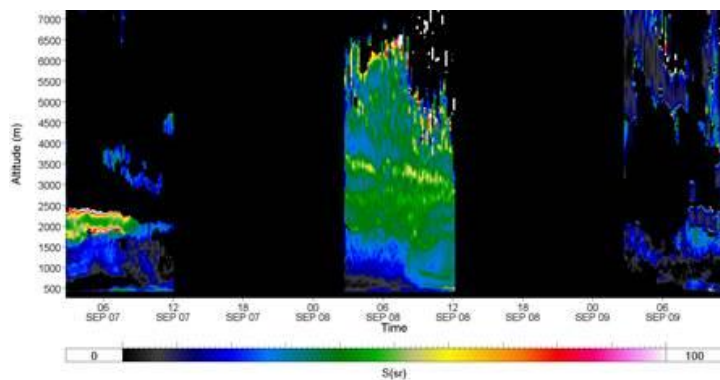


2

3



4

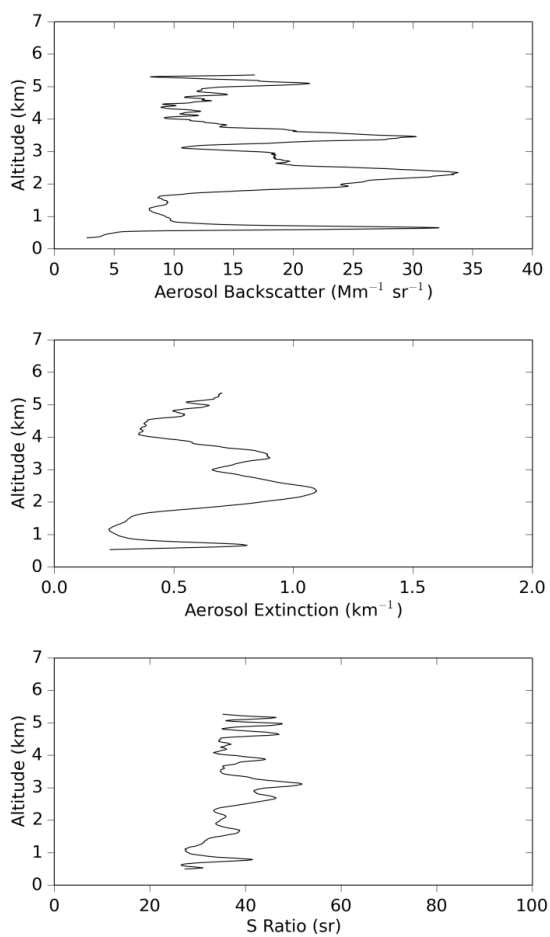


5

6



1 Fig. 23

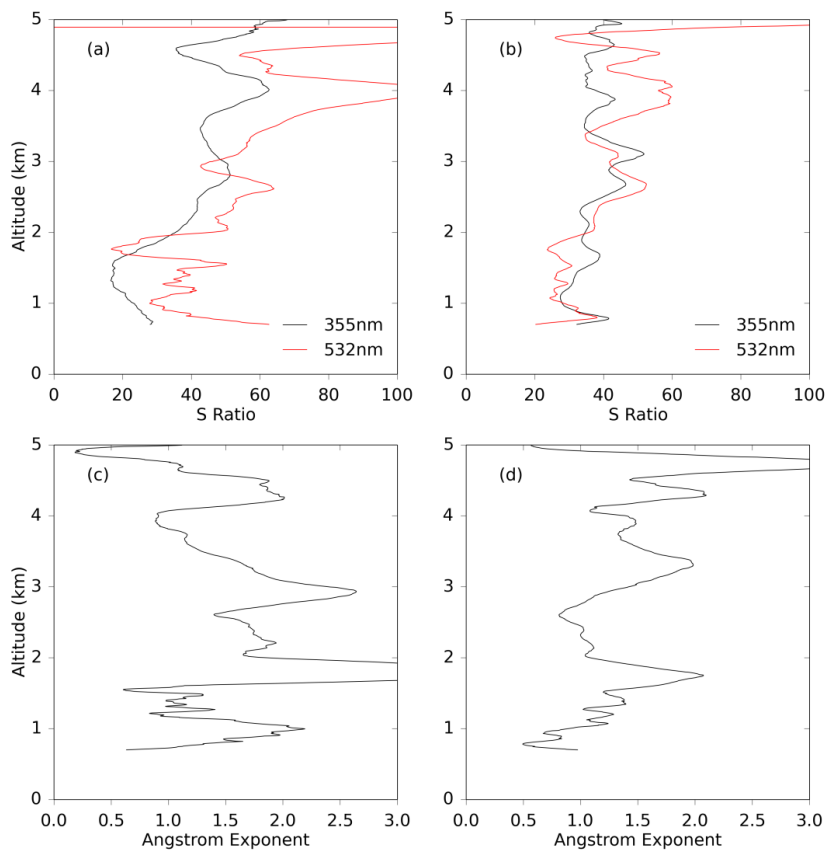


2

3



1 Fig. 24



2